Commun. Comput. Phys.
doi: 10.4208/cicp.130114.270315a

Vol. **18**, No. 5, pp. 1282-1312
November 2015

A Numerical Scheme for Generalized Peierls-Nabarro Model of Dislocations Based on the Fast Multipole Method and Iterative Grid Redistribution

Aiyu Zhu[1], Congming Jin[2], Degang Zhao[3], Yang Xiang[1,*] and Jingfang Huang[4]

[1] *Department of Mathematics, The Hong Kong University of Science and Technology, Clear Water Bay, Kowloon, Hong Kong.*
[2] *Department of Mathematics, Zhejiang Sci-Tech University, Zhejiang, China.*
[3] *School of Physics, Huazhong University of Science and Technology, Wuhan 430074, China.*
[4] *Department of Mathematics, The University of North Carolina at Chapel Hill, Chapel Hill, NC 27599-3250, USA.*

Received 13 January 2014; Accepted (in revised version) 27 March 2015

Abstract. Dislocations are line defects in crystalline materials. The Peierls-Nabarro models are hybrid models that incorporate atomic structure of dislocation core into continuum framework. In this paper, we present a numerical method for a generalized Peierls-Nabarro model for curved dislocations, based on the fast multipole method and the iterative grid redistribution. The fast multipole method enables the calculation of the long-range elastic interaction within operations that scale linearly with the total number of grid points. The iterative grid redistribution places more mesh nodes in the regions around the dislocations than in the rest of the domain, thus increases the accuracy and efficiency. This numerical scheme improves the available numerical methods in the literature in which the long-range elastic interactions are calculated directly from summations in the physical domains; and is more flexible to handle problems with general boundary conditions compared with the previous FFT based method which applies only under periodic boundary conditions. Numerical examples using this method on the core structures of dislocations in Al and Cu and in epitaxial thin films are presented.

AMS subject classifications: 65R20, 65N50, 74A50, 74G65

Key words: Dislocation, elasticity, Peierls-Nabarro model, iterative grid redistribution, fast multipole method.

*Corresponding author. *Email addresses:* maayzhu@ust.hk (A. Zhu), jincm@lsec.cc.ac.cn (C. Jin), dgzhao@hust.edu.cn (D. Zhao), maxiang@ust.hk (Y. Xiang), huang@email.unc.edu (J. Huang)

1 Introduction

Dislocations are line defects and the primary carriers of plastic deformation in crystalline materials. In the dislocation theory, the elastic field of a dislocation is very well described by the continuum linear elasticity theory outside a small region surrounding the dislocation [1]. Inside the small region around the dislocation, which is known as the core region of the dislocation, the atomic structure is heavily distorted, and the linear elasticity theory gives unphysical singularities in the elastic field. The core region determines the energy and the mobility of the dislocation, thus its modeling plays important roles in the dislocation and plasticity theories. The Peierls-Nabarro model [1–3] provides a way to incorporates atomic features inside the core region into the continuum linear elasticity theory. More accurate first principles results can also be included in the framework of the Peierls-Nabarro model [5,10–12,15,17] through the generalized stacking fault energy [4].

In the Peierls-Nabarro model [1–3], the solid is divided by the slip plane of the dislocation into two half-space linear elastic continua, with a disregistry (or misfit) relative to each other and connected by a nonlinear potential force. The total energy consists of the elastic energy in the two half-space continua and the misfit energy due to the nonlinear atomic interaction across the slip plane. The dislocation core profile is determined by energy minimization. The solution of the Peierls-Nabarro model gives a description for the dislocation core profile as well as the energy barrier (Peierls energy) and the critical stress (Peierls stress) for the motion of dislocations. Previously, efforts were made mainly on straight dislocations [2–15,17,19,20].

Several generalized Peierls-Nabarro models for curved dislocations have been proposed [16, 18, 21–23]. Some recent applications of the Peierls-Nabarro models can be found, e.g., in [24–29]. The major numerical challenge of such models lies in the calculation of the long-range elastic interaction. In the finite element based model proposed in [16], this long-range interaction is calculated by direct summation over all the grid points, which requires $\mathcal{O}(N^2)$ operations, where N is the total number of grid points [30]. The lattice model presented in [18] also requires $\mathcal{O}(N^2)$ direct summation for the long-range interaction of dislocation over the slip plane with N lattice sites. The models proposed in [21–23] employ the fast Fourier transform method (FFT) for the generalized Peierls-Nabarro on a uniform mesh with periodic boundary conditions, thus only $\mathcal{O}(N\log N)$ operations are needed for the calculation of this long-range interaction. Although the FFT based generalized Peierls-Nabarro models are quite efficient, they are limited to periodic boundary conditions which mimic the behavior of dislocations in bulk of the materials. However, the periodic boundary conditions cannot be used when materials boundaries are present, for example, when dislocations are in thin films where traction-free boundary conditions are required on the free surfaces [6,7].

In this paper, we present an alternative numerical method for the generalized Peierls-Nabarro model in Ref. [21] based on the fast multipole method (FMM) [33,34] and the iterative grid redistribution [35]. This presented numerical method is an improvement of the available numerical methods in the literature in which the long-range elastic interac-

tions are calculated directly from summations in the physical domains with $\mathcal{O}(N^2)$ operations [7,10,13,15–18], and has the advantage of being more flexible to handle problems with general boundary conditions especially when materials boundaries are present. In fact, the FMM enables the calculation of the long-range elastic interaction within $\mathcal{O}(N)$ operations. The iterative grid redistribution places more mesh nodes in the regions around the dislocations than in the rest of the domain, thus increases the accuracy (with the same number of grid points) or efficiency (with the same resolution), and this grid redistribution is also achieved with computational cost of $\mathcal{O}(N)$.

We apply the developed numerical method to dislocations in Al (in which dislocations have narrow cores) and Cu (in which dislocations have wide cores) under isotropic elasticity. We have also presented numerical examples of the core profile of a straight edge dislocation on the interface of epitaxial thin film and substrate, where the image stress due to the free surface is not negligible. Generalizations to anisotropic elasticity [21] and dislocations in materials with the effect of image stress due to boundaries [1, 6,7,37–39] are being considered and will be presented elsewhere.

The rest of the paper is organized as follows. In Section 2, we review the generalized Peierls-Nabarro model for curved dislocations. In Section 3, we present our numerical method for generalized Peierls-Nabarro model of dislocations based on the fast multipole method and iterative grid redistribution. Numerical examples including straight dislocations and dislocation loops in Al and Cu and a straight edge dislocation on the interface of epitaxial thin film and substrate are presented in Section 4. Derivation of higher order corrections from the local integrals with singularities in the evaluation of the stress field is presented in the appendix.

2 The generalized Peierls-Nabarro model

In this section, we review the formulation of the generalized Peierls-Nabarro model for curved dislocations [21], based on which our numerical method is developed.

In the framework of the Peierls-Nabarro model, the crystal is divided by the slip plane of the dislocation into two half-spaces. Linear elasticity theory applies in each half-space, and the two half-spaces are connected by an atomic potential force.

Suppose that the slip plane of the dislocation is located at $z=0$. In the linear elasticity theory in the half-spaces $z>0$ and $z<0$, the strain tensor is defined in terms of the displacement vector (u_1,u_2,u_3):

$$\epsilon_{ij}=\frac{1}{2}\left(\frac{\partial u_j}{\partial x_i}+\frac{\partial u_i}{\partial x_j}\right),\quad i,j=1,2,3, \tag{2.1}$$

and the stress tensor is determined from the strain tensor by the constitutive equations

$$\sigma_{ij}=\sum_{k,l=1}^{3} C_{ijkl}\epsilon_{kl},\quad i,j=1,2,3, \tag{2.2}$$

where $\{C_{ijkl}\}$ is the elastic constant tensor. In an isotropic medium, the constitutive equations are

$$\sigma_{ij}=2\mu\epsilon_{ij}+\frac{2\nu\mu}{1-\nu}(\epsilon_{11}+\epsilon_{22}+\epsilon_{33})\delta_{ij},\quad i,j=1,2,3, \tag{2.3}$$

where μ is the shear modulus, ν is the Poisson ratio, and $\delta_{ij}=1$ if $i=j$ and 0 otherwise. In addition, the following equilibrium conditions hold without body force:

$$\nabla\cdot\sigma=0. \tag{2.4}$$

The elastic energy in the two half-space is

$$E_{\text{elastic}}=\int_{R^3}\sum_{i,j=1}^{3}\frac{1}{2}\sigma_{ij}\epsilon_{ij}dxdydz. \tag{2.5}$$

Along any loop enclosing a dislocation line, the displacement vector increases by a constant vector, which is the Burgers vector **b** of the dislocation. This discontinuity associated with the dislocation generates a stress field over the whole medium, which is singular on the dislocation within the linear elasticity theory. This singularity is not physical due to the breakdown of the linear elasticity theory insider the core region of the dislocation. In the framework of the Peierls-Nabarro model, the Burgers vector **b** is assumed to spread out within the core region in the slip plane, and such spread-out is determined by the local nonlinear atomic interaction across the slip plane. The energy due to the nonlinear atomic interaction across the slip plane, referred to as the misfit energy, is

$$E_{\text{misfit}}=\int_{R^2}\gamma(\phi(x,y),\psi(x,y))dxdy, \tag{2.6}$$

where $\gamma(\phi,\psi)$ is the generalized stacking fault energy [4], defined as the energy increment per unit area when there is a relative shift of displacement across the slip plane, referred to as the disregistry:

$$(\phi(x,y),\psi(x,y),0)=(u_1(x,y,0^+)-u_1(x,y,0^-),u_2(x,y,0^+)-u_2(x,y,0^-),0). \tag{2.7}$$

The generalized stacking fault energy γ can be obtained from atomistic models or first principles calculations. It has the minimum value when the disregistry is an integer multiple of the Burgers vector **b**, and its local minima correspond to the stacking fault region (leading to dislocation partial dissociation), see Fig. 1. In the Peierls-Nabarro model, it is further assumed that $u_1(x,y,0^-)=-u_1(x,y,0^+)$, $u_2(x,y,0^-)=-u_2(x,y,0^+)$, and $u_3(x,y,0^-)=u_3(x,y,0^+)$.

The equilibrium configuration of the dislocation can be found by minimizing the total energy

$$E=E_{\text{elastic}}+E_{\text{misfit}}. \tag{2.8}$$

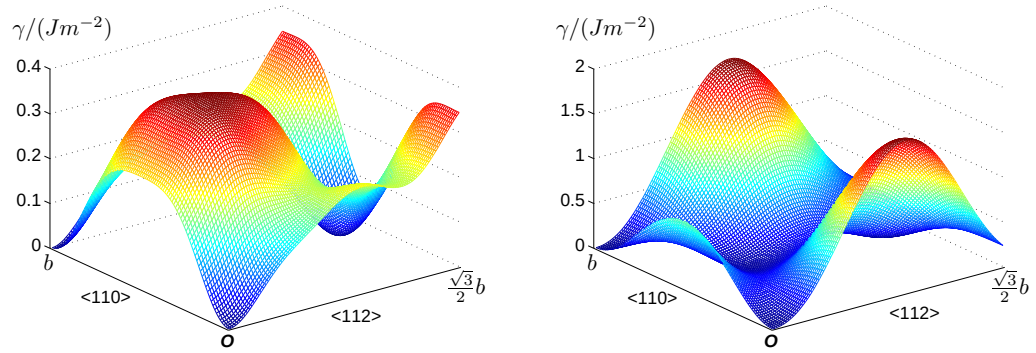

(a) (b)

Figure 1: The generalized stacking fault energy $\gamma(\phi,\psi)$. (a) $\gamma(\phi,\psi)$ on Al (111) plane and (b) $\gamma(\phi,\psi)$ on Cu (111) plane.

Taking variation of the total energy, we have the following equations for the equilibrium configuration of the dislocation:

$$\frac{\partial E}{\partial \phi}=\sigma_{13}+\frac{\partial \gamma}{\partial \phi}=0, \quad \frac{\partial E}{\partial \psi}=\sigma_{23}+\frac{\partial \gamma}{\partial \psi}=0, \tag{2.9}$$

where σ_{13} and σ_{23} are stress components on the slip plane z=0. The solutions $\phi(x,y),\psi(x,y)$ can be found by solving the following evolution equations which minimize the total energy in the steepest descent direction to the equilibrium state

$$\begin{aligned}\frac{\partial \phi}{\partial t}&=-M\left(\sigma_{13}+\frac{\partial \gamma}{\partial \phi}\right),\\ \frac{\partial \psi}{\partial t}&=-M\left(\sigma_{23}+\frac{\partial \gamma}{\partial \psi}\right),\end{aligned} \tag{2.10}$$

where M is some positive constant.

Under applied stress $(\sigma_{13}^{\text{app}},\sigma_{23}^{\text{app}})$, the equilibrium configuration of the dislocation is determined by minimizing the total energy:

$$E=E_{\text{elastic}}+E_{\text{misfit}}+\int_{R^2}(\sigma_{13}^{\text{app}}\phi+\sigma_{23}^{\text{app}}\psi)dxdy. \tag{2.11}$$

The resulting equations in equilibrium are

$$\sigma_{13}+\frac{\partial \gamma}{\partial \phi}+\sigma_{13}^{\text{app}}=0, \quad \sigma_{23}+\frac{\partial \gamma}{\partial \psi}+\sigma_{23}^{\text{app}}=0, \tag{2.12}$$

and the solution can be found by solving the following evolution equations to the equilibrium state:

$$\begin{aligned}\frac{\partial\phi}{\partial t}&=-M\left(\sigma_{13}+\frac{\partial\gamma}{\partial\phi}+\sigma_{13}^{\text{app}}\right),\\ \frac{\partial\psi}{\partial t}&=-M\left(\sigma_{23}+\frac{\partial\gamma}{\partial\psi}+\sigma_{23}^{\text{app}}\right),\end{aligned}\tag{2.13}$$

for some positive constant M.

In this paper, we focus on the case of isotropic elasticity, which gives the following formulas for the stress components in terms of ϕ and ψ [1,21]:

$$\begin{aligned}\sigma_{13}(x,y)=\int_{R^2}\Bigg\{&\frac{\mu}{4\pi}\frac{y-y_1}{[(x-x_1)^2+(y-y_1)^2]^{3/2}}\phi_y(x_1,y_1)\\&+\frac{\mu}{4\pi(1-\nu)}\frac{x-x_1}{[(x-x_1)^2+(y-y_1)^2]^{3/2}}\phi_x(x_1,y_1)\\&+\frac{\mu\nu}{4\pi(1-\nu)}\frac{x-x_1}{[(x-x_1)^2+(y-y_1)^2]^{3/2}}\psi_y(x_1,y_1)\Bigg\}dx_1dy_1,\end{aligned}\tag{2.14}$$

and

$$\begin{aligned}\sigma_{23}(x,y)=\int_{R^2}\Bigg\{&\frac{\mu\nu}{4\pi(1-\nu)}\frac{y-y_1}{[(x-x_1)^2+(y-y_1)^2]^{3/2}}\phi_x(x_1,y_1)\\&+\frac{\mu}{4\pi}\frac{x-x_1}{[(x-x_1)^2+(y-y_1)^2]^{3/2}}\psi_x(x_1,y_1)\\&+\frac{\mu}{4\pi(1-\nu)}\frac{y-y_1}{[(x-x_1)^2+(y-y_1)^2]^{3/2}}\psi_y(x_1,y_1)\Bigg\}dx_1dy_1.\end{aligned}\tag{2.15}$$

Note that these stress components depend on the partial derivatives of the disregistry functions ϕ and ψ. More precisely, the stress depends on the Nye dislocation density tensor, which in this case is [21,31]

$$\{\alpha_{ij}\}=\begin{pmatrix}\phi_y(x,y)\delta(z) & \psi_y(x,y)\delta(z) & 0\\ -\phi_x(x,y)\delta(z) & -\psi_x(x,y)\delta(z) & 0\\ 0 & 0 & 0\end{pmatrix},\tag{2.16}$$

where $\delta(z)$ is the Dirac delta function of the $z=0$ plane.

In the numerical examples in this paper, we calculate dislocation core structures in Al and Cu. The metals Al and Cu have the face-centred cubic (fcc) atomic lattice. The dislocations in an fcc crystal have Burgers vectors $\mathbf{b}=\frac{a}{2}<110>$ where a is the lattice constant, and slip planes of $\{111\}$ type. Here we choose the x, y, and z coordinate axes in the directions $[\bar{1}10]$, $[\bar{1}\bar{1}2]$, and $[111]$, respectively. The slip plane $z=0$ is a (111) plane, and the Burgers vector is in the x direction: $\mathbf{b}=\frac{a}{2}[\bar{1}10]$. The length of Burgers vector $b=2.86\mathring{A}$

in Al and $b=2.55\mathring{A}$ in Cu. The elastic constants are $\mu=2.65\times10^{10}Pa$ and $\nu=0.347$ in Al, and $\mu=5.46\times10^{10}Pa$ and $\nu=0.324$ in Cu. These parameters can be found, e.g. in Ref. [1].

For Al and Cu, the generalized stacking fault energy is [21]:

$$\begin{aligned}\gamma(\phi,\psi)=c_0+c_1&\left[\cos\frac{2\pi}{b}(\phi+\psi/\sqrt{3})+\cos\frac{2\pi}{b}(\phi-\psi/\sqrt{3})+\cos(\frac{4\pi\psi}{\sqrt{3}b})\right]\\&+c_2\left[\cos\frac{2\pi}{b}(\phi+\sqrt{3}\psi)+\cos\frac{2\pi}{b}(\phi-\sqrt{3}\psi)+\cos\frac{4\pi}{b}\right]\\&+c_3\left[\cos\frac{2\pi}{b}(2\phi+2\psi/\sqrt{3})+\cos\frac{2\pi}{b}(2\phi-2\psi/\sqrt{3})+\cos\frac{8\pi\psi}{\sqrt{3}b}\right]\\&+d_1\left[\sin\frac{2\pi}{b}(\phi-\psi/\sqrt{3})-\sin\frac{2\pi}{b}(\phi+\psi/\sqrt{3})+\sin\frac{4\pi\psi}{\sqrt{3}b}\right]\\&+d_2\left[\sin\frac{2\pi}{b}(2\phi-2\psi/\sqrt{3})-\sin\frac{2\pi}{b}(2\phi+2\psi/\sqrt{3})+\sin\frac{8\pi\psi}{\sqrt{3}b}\right].\end{aligned}\tag{2.17}$$

Here ϕ is the disregistry in the direction of the Burgers vector **b** (the x direction) and has a jump of b across the core region of the dislocation, whereas ψ is the disregistry in the direction normal to **b** in the slip plane (the y direction). Roughly speaking, the disregistry function ϕ determines the location of the dislocation, and the disregistry function ψ is associated with the partial dissociation within the dislocation core [1,21].

In Eq. (2.17), the parameter $c_0=-3c_1-3c_2-3c_3$. For Al, the coefficients $c_1=-0.0577Jm^{-2}$, $c_2=-0.0048Jm^{-2}$, $c_3=-0.0115Jm^{-2}$, $d_1=0.0424Jm^{-2}$, $d_2=0.0135Jm^{-2}$; and for Cu, $c_1=-0.1866Jm^{-2}$, $c_2=0$, $c_3=-0.0076Jm^{-2}$, $d_1=-0.32324Jm^{-2}$, $d_2=-0.0042Jm^{-2}$. These values of the coefficients are obtained by fitting available data for the elastic constants in the (111) plane (in an isotropic medium), for the stacking fault energy, for the unstable stacking fault energy in the $<112>$ directions and for the unstable stacking fault energy in the $<110>$ directions [1,15,21,32]. The obtained $\gamma(\phi,\psi)$ for Al and Cu are shown in Fig. 1.

Besides the periodic boundary condition [21], another boundary condition commonly adopted in the Peierls-Nabarro models in the literature is that the dislocation profile is spread only within the simulation domain [10,13,15–18]. This condition is equivalent to $\nabla\phi=\nabla\psi=\mathbf{0}$ outside the simulation domain, see the Nye dislocation density tensor in Eq. (2.16). This can be implemented by the Neumann boundary conditions for ϕ and ψ in the Peierls-Nabarro model in a finite domain. We will focus on this boundary condition in this paper. Other boundary conditions can also be easily imposed using our numerical method presented in the next section.

3 The numerical method

In the formulation of the generalized Peierls-Nabarro model in the previous section, we solve the evolution equations of ϕ and ψ in Eq. (2.10) (or (2.13) under the applied stress)

to equilibrium state, with stress components being calculated using Eq. (2.14) and (2.15) and the generalized stacking fault energy using Eq. (2.17). In this section, we present an efficient numerical method to solve these evolution equations. In this method, the stress components in Eqs. (2.14) and (2.15) are calculated using the fast multipole method (FMM) [33, 34], and the evolution equations in Eq. (2.10) or (2.13) are solved on an adaptive mesh generated by the iterative grid redistribution technique [35].

3.1 Iterative grid redistribution

In the generalized Peierls-Nabarro model, the disregistry functions ϕ and ψ vary rapidly within the dislocation core region, and quickly approach constants outside the core. Based on this property, we use the variation-based grid redistribution method [35, 36] to generate an adaptive mesh for solving the evolution equations of ϕ and ψ.

The computational domain $(\xi,\eta)\in\Omega_c$ is discretized into a uniform mesh, and the physical domain $(x,y)\in\Omega_p$ is adaptive. There is a one-to-one mapping (the Winslow mapping) from the physical domain Ω_p to the computational domain Ω_c:

$$\begin{aligned}\mathbf{T}: \quad & (x,y)\longrightarrow(\xi,\eta),\\ & (\phi(x,y),\psi(x,y))\longrightarrow(\phi^c(\xi,\eta),\psi^c(\xi,\eta)),\end{aligned}\tag{3.1}$$

where $\phi^c(\xi,\eta)=\phi(x(\xi,\eta),y(\xi,\eta))$ and $\psi^c(\xi,\eta)=\psi(x(\xi,\eta),y(\xi,\eta))$. The mapping is determined by minimizing the energy

$$E(\xi,\eta)=\int_{\Omega_p}\frac{1}{w}(|\nabla_p\,\xi|^2+|\nabla_p\,\eta|^2)dxdy,\tag{3.2}$$

where ∇_p (and also Δ_p in Eq. (3.3)) denotes the operator with respect to variables (x,y) in the physical domain, and $\omega>0$ is a weight function. The weight function w reflects the features of the solutions, and in the generalized Peierls-Nabarro model, we choose

$$w(x,y)=\sqrt{1+\alpha|\phi(x,y)|+\beta|\nabla_p\,\phi(x,y)|+\gamma|\Delta_p\phi(x,y)|},\tag{3.3}$$

where $\alpha,\beta,\gamma>0$ are some constants. With this weight function w, more mesh grid points over the physical domain are moved into the dislocation core region. We use ϕ in the weight function because it is the disregistry in the direction of the Burgers vector and is able to characterize the dislocation core region.

The mapping that minimizes energy E satisfies the Euler-Lagrange equations

$$\begin{aligned}&\nabla_p\cdot\left(\frac{1}{w}\nabla_p\,\xi\right)=0,\\ &\nabla_p\cdot\left(\frac{1}{w}\nabla_p\,\eta\right)=0.\end{aligned}\tag{3.4}$$

A method to find the solutions of the elliptic equations (3.4) is to solve the gradient flow equations to equilibrium state

$$\begin{aligned}\frac{\partial\xi}{\partial\tau}-\nabla_p\cdot\left(\frac{1}{w}\nabla_p\,\xi\right)&=0,\\ \frac{\partial\eta}{\partial\tau}-\nabla_p\cdot\left(\frac{1}{w}\nabla_p\,\eta\right)&=0,\end{aligned}\tag{3.5}$$

where τ is some artificial time. In actual computation, the dependent and independent variables in Eq. (3.4) are interchanged, i.e. the following evolution equations over the computational domain are solved to equilibrium state to obtain the mapping:

$$\begin{aligned}x_\tau&=\frac{x_\xi}{J}\left[\frac{\partial}{\partial\xi}\left(\frac{x_\eta^2+y_\eta^2}{Jw}\right)-\frac{\partial}{\partial\eta}\left(\frac{x_\xi x_\eta+y_\xi y_\eta}{Jw}\right)\right]-\frac{x_\eta}{J}\left[\frac{\partial}{\partial\xi}\left(\frac{x_\xi x_\eta+y_\xi y_\eta}{Jw}\right)-\frac{\partial}{\partial\eta}\left(\frac{x_\xi^2+y_\xi^2}{Jw}\right)\right]\\ y_\tau&=\frac{y_\xi}{J}\left[\frac{\partial}{\partial\xi}\left(\frac{x_\eta^2+y_\eta^2}{Jw}\right)-\frac{\partial}{\partial\eta}\left(\frac{x_\xi x_\eta+y_\xi y_\eta}{Jw}\right)\right]-\frac{y_\eta}{J}\left[\frac{\partial}{\partial\xi}\left(\frac{x_\xi x_\eta+y_\xi y_\eta}{Jw}\right)-\frac{\partial}{\partial\eta}\left(\frac{x_\xi^2+y_\xi^2}{Jw}\right)\right],\end{aligned}\tag{3.6}$$

where $J=x_\xi y_\eta-x_\eta y_\xi$ is the Jacobian of the mapping.

We use the iterative grid redistribution method [35] to determine the mapping numerically during the evolution of the disregistry functions ϕ and ψ. The advantage of this iterative method is that it is able to achieve precise control of the grid distribution near regions of large solution variations. The idea of this method is to use the Winslow mapping iteratively

$$\begin{array}{ccccccc}(x,y) & \longrightarrow & (\xi^1,\eta^1) & \longrightarrow & (\xi^2,\eta^2) & \cdots\\ (\phi(x,y),\psi(x,y)) & \longrightarrow & (\phi^1(\xi^1,\eta^1),\psi^1(\xi^1,\eta^1)) & \longrightarrow & (\phi^2(\xi^2,\eta^2),\psi^2(\xi^2,\eta^2)) & \cdots.\end{array}\tag{3.7}$$

It has been shown [35] that as $k\to\infty$,

$$\begin{aligned}(\xi^k,\eta^k) &\to (\xi,\eta),\\ (\phi^k(\xi^k,\eta^k),\psi^k(\xi^k,\eta^k)) &\to (\phi(x(\xi,\eta),y(\xi,\eta)),\psi(x(\xi,\eta),y(\xi,\eta))),\end{aligned}\tag{3.8}$$

which gives the desired grid redistribution under the given weight function w.

The algorithm of this iteration process is as follows:

Step 1: Let (ξ^k,η^k) and $(\phi^k(\xi^k,\eta^k),\psi^k(\xi^k,\eta^k))$ be the mesh and disregistry vector, respectively, after k iterations.

Step 2: Determine (ξ^{k+1},η^{k+1}) from (ξ^k,η^k) and $(\phi^k(\xi^k,\eta^k),\psi^k(\xi^k,\eta^k))$ using Eq. (3.5) (in which $(x,y)=(\xi^k,\eta^k)$ and $(\xi,\eta)=(\xi^{k+1},\eta^{k+1})$).

Step 3: Define $\phi^{k+1}(\xi^{k+1},\eta^{k+1})=\phi^k(\xi^k(\xi^{k+1},\eta^{k+1}),\eta^k(\xi^{k+1},\eta^{k+1}))$, $\psi^{k+1}(\xi^{k+1},\eta^{k+1})=\psi^k(\xi^k(\xi^{k+1},\eta^{k+1}),\eta^k(\xi^{k+1},\eta^{k+1}))$, and $x(\xi^{k+1},\eta^{k+1})=x(\xi^k(\xi^{k+1},\eta^{k+1}),\eta^k(\xi^{k+1},\eta^{k+1}))$, $y(\xi^{k+1},\eta^{k+1})=y(\xi^k(\xi^{k+1},\eta^{k+1}),\eta^k(\xi^{k+1},\eta^{k+1}))$. Go to Step 1.

The iteration stops when $|\nabla_c \phi| < TOL$.

We use Dirichlet boundary conditions for the moving mesh equations, in which the redistributed mesh remains uniform on the domain boundaries, following Ref. [35].

3.2 Numerical discretization of PDEs and calculation of stress using FMM

We solve the evolution equations of ϕ and ψ in Eq. (2.13) on a rectangular physical domain Ω_p with the adaptive mesh described in the previous subsection. The computational domain Ω_c is rectangular and a uniform $M_1 \times M_2$ mesh $\{(\xi_i,\eta_j),\ i=0,\cdots,M_1,\ j=0,\cdots,M_2\}$ is given on it. Accordingly, the physical domain Ω_p is discretized into a $M_1 \times M_2$ adaptive mesh. The discretization of the evolution equations in Eq. (2.13) is

$$\begin{aligned}
\frac{\phi_{i,j}^{n+1}-\phi_{i,j}^{n}}{\Delta t} &= -(\sigma_{13})_{i,j}^{n} - \left(\frac{\partial \gamma}{\partial \phi}\right)_{i,j}^{n} - \sigma_{13}^{app}, \\
\frac{\psi_{i,j}^{n+1}-\psi_{i,j}^{n}}{\Delta t} &= -(\sigma_{23})_{i,j}^{n} - \left(\frac{\partial \gamma}{\partial \psi}\right)_{i,j}^{n} - \sigma_{23}^{app},
\end{aligned} \tag{3.9}$$

where the notation $f_{i,j}^{n} = f(x_i,y_j,t_n)$ for a function f defined on $\Omega_c \times [0,\infty)$, and Δt is the time step size.

The stress components $(\sigma_{13})_{i,j}^{n}$ and $(\sigma_{23})_{i,j}^{n}$ are numerical approximations of the integral expressions in Eqs. (2.14) and (2.15) in the computational domain Ω_c:

$$\begin{aligned}
(\sigma_{13})_{i,j}^{n} = & \sum_{\substack{0\le i_1\le M_1\\ 0\le j_1\le M_2\\ (i_1,j_1)\neq(i,j)}} \left\{ \frac{\mu}{4\pi} \frac{y_{i,j}^{n}-y_{i_1,j_1}^{n}}{[(x_{i,j}^{n}-x_{i_1,j_1}^{n})^2+(y_{i,j}^{n}-y_{i_1,j_1}^{n})^2]^{3/2}} \left(\frac{-\phi_\xi x_\eta+\phi_\eta x_\xi}{J}\right)_{i_1,j_1}^{n} \right. \\
& + \frac{\mu}{4\pi(1-\nu)} \frac{x_{i,j}^{n}-x_{i_1,j_1}^{n}}{[(x_{i,j}^{n}-x_{i_1,j_1}^{n})^2+(y_{i,j}^{n}-y_{i_1,j_1}^{n})^2]^{3/2}} \left(\frac{\phi_\xi y_\eta-\phi_\eta y_\xi}{J}\right)_{i_1,j_1}^{n} \\
& \left. + \frac{\mu\nu}{4\pi(1-\nu)} \frac{x_{i,j}^{n}-x_{i_1,j_1}^{n}}{[(x_{i,j}^{n}-x_{i_1,j_1}^{n})^2+(y_{i,j}^{n}-y_{i_1,j_1}^{n})^2]^{3/2}} \left(\frac{-\psi_\xi x_\eta+\psi_\eta x_\xi}{J}\right)_{i_1,j_1}^{n} \right\} |J_{i,j}^{n}| h_1 h_2 \\
& + (s_1)_{i,j}^{n},
\end{aligned} \tag{3.10}$$

$$\begin{aligned}
(\sigma_{23})_{i,j}^{n} = & \sum_{\substack{0\le i_1\le M_1\\ 0\le j_1\le M_2\\ (i_1,j_1)\neq(i,j)}} \left\{ \frac{\mu\nu}{4\pi(1-\nu)} \frac{y_{i,j}^{n}-y_{i_1,j_1}^{n}}{[(x_{i,j}^{n}-x_{i_1,j_1}^{n})^2+(y_{i,j}^{n}-y_{i_1,j_1}^{n})^2]^{3/2}} \left(\frac{\phi_\xi y_\eta-\phi_\eta y_\xi}{J}\right)_{i_1,j_1}^{n} \right. \\
& + \frac{\mu}{4\pi} \frac{x_{i,j}^{n}-x_{i_1,j_1}^{n}}{[(x_{i,j}^{n}-x_{i_1,j_1}^{n})^2+(y_{i,j}^{n}-y_{i_1,j_1}^{n})^2]^{3/2}} \left(\frac{\psi_\xi y_\eta-\psi_\eta y_\xi}{J}\right)_{i_1,j_1}^{n} \\
& \left. + \frac{\mu}{4\pi(1-\nu)} \frac{y_{i,j}^{n}-y_{i_1,j_1}^{n}}{[(x_{i,j}^{n}-x_{i_1,j_1}^{n})^2+(y_{i,j}^{n}-y_{i_1,j_1}^{n})^2]^{3/2}} \left(\frac{-\psi_\xi x_\eta+\psi_\eta x_\xi}{J}\right)_{i_1,j_1}^{n} \right\} |J_{i,j}^{n}| h_1 h_2 \\
& + (s_2)_{i,j}^{n},
\end{aligned} \tag{3.11}$$

for $i=0,1,2,\cdots,M_1$ and $j=0,1,2,\cdots,M_2$, where $J=x_\xi y_\eta - x_\eta y_\xi$ is the Jacobian of the mapping, h_1 and h_2 are the grid constants in the direction of ξ and η, respectively, and $(s_1)^n_{i,j}$, $(s_2)^n_{i,j}$ are contributions from the local singular integrals (see the paragraph below) whose formulas will be given in the next subsection in Eqs. (3.14) and (3.15). The partial derivatives with respect to ξ and η are calculated by the central difference scheme. In this paper, we use Neumann boundary conditions. Accordingly, $\phi_{-1,j_1}=\phi_{0,j_1}$, $\phi_{M_1+1,j_1}=\phi_{M_1,j_1}$, $\phi_{i_1,-1}=\phi_{i_1,0}$, $\phi_{i_1,M_2+1}=\phi_{i_1,M_2}$ when the formers are needed in the central difference scheme for its partial derivatives, and same for ψ.

In fact, Eqs. (3.10) and (3.11) are discretizations of the corresponding integral formulas in Eqs. (2.14) and (2.15) by constant approximation over each small cell in the computational domain $[\xi_{i_1,j_1}-\frac{h_1}{2},\xi_{i_1,j_1}+\frac{h_1}{2}]\times[\eta_{i_1,j_1}-\frac{h_2}{2},\eta_{i_1,j_1}+\frac{h_2}{2}]$. The singular integrals over the small cells when $(i_1,j_1)=(i,j)$, denoted by $(s_1)^n_{i,j}$ and $(s_2)^n_{i,j}$ in Eqs. (3.10) and (3.11), respectively, will be discussed in the next subsection. To obtain Eqs. (3.10) and (3.11), we have also used

$$\begin{aligned}\phi_x&=\frac{\phi_\xi y_\eta-\phi_\eta y_\xi}{J},\\ \phi_y&=\frac{-\phi_\xi x_\eta+\phi_\eta x_\xi}{J},\end{aligned}\tag{3.12}$$

and same for the partial derivatives of ψ.

We calculate the summations in the stress components in Eqs. (3.10) and (3.11) using the fast multipole method (FMM) [33,34]. Due to the double summations in these formulas, a direct summation method requires $\mathcal{O}(N^2)$ operations, where $N=(M_1+1)(M_2+1)$ is the total number of grid points. We use the new version FMM for evaluating the stress field of dislocation ensembles developed in Ref. [34] to calculate these double summations, whose computational cost is asymptotically $\mathcal{O}(N)$ with an optimized prefactor. The method developed in Ref. [34] is to calculate the long-range stress field of three-dimensional distributions of dislocations, which takes the following form after discretization of integrals along all the dislocations:

$$\sigma_{ij}(\mathbf{X}_h)=\sum_{l,r,s,t} q^{(ij)}_{lrst} R_{,rst}(\mathbf{X}_h-\mathbf{X}^*_l),\tag{3.13}$$

where $\mathbf{X}_h$, $h=1,2,\cdots,N_0$, are the target points on the dislocations, $\mathbf{X}^*_l$, $l=1,2,\cdots,N^*$, are the source points on the dislocations, $R(\mathbf{X}_h-\mathbf{X}^*_l)$ is the distance between the two points $\mathbf{X}_h$ and $\mathbf{X}^*_l$, $R_{,ijk}$ is the third order partial derivative of R with respect to spatial variables defined as $R_{,ijk}=\partial^3 R/\partial x_i\partial x_j\partial x_k$ (where x_1, x_2 and x_3 are three coordinate variables), and $q^{(ij)}_{lrst}$ is a coefficient depending on the Burgers vector and unit tangent vector of the dislocation at $\mathbf{X}^*_l$. More details of this method can be found in Ref. [34]. Here the distribution of dislocations in the Peierls-Nabarro model with discrete stress formulas in Eqs. (3.10) and (3.11) is a special case in which all the target and source points are located in a single slip plane.

In summary of our numerical method for the generalized Peierls-Nabarro model, we first generate an initial adaptive mesh (the Winslow mapping) using the iterative grid redistribution method in Section 3.1 and the initial conditions of ϕ an ψ. Then the evolution equations of ϕ and ψ are solved in the computational domain $(\xi,\eta)\in\Omega_c$ using the scheme in Eq. (3.9) until $\max|\nabla_c\phi|>TOL$, where TOL is some prescribed number. During the evolution, the stress components in Eq. (3.9) are calculated by Eqs. (3.10) and (3.11) using FMM. When $\max|\nabla_c\phi|>TOL$ happens, a new adaptive mesh is obtained using the iterative grid redistribution method. The evolution in Eq. (3.9) is then continued on the new adaptive mesh. This procedure repeats until an equilibrium state of dislocation structure is reached.

3.3 Local integrals with singularities

In this subsection, we discuss the terms $(s_1)^n_{i,j}$ and $(s_2)^n_{i,j}$ in Eqs. (3.10) and (3.11), which are the approximations respectively of the integrals in Eqs. (2.14) and (2.15) over the small region $D^p_{i,j}$ containing the point $(x_{i,j},y_{i,j})$ and mapped from the small region $(\xi_1,\eta_1)\in D^c_{i,j}=[\xi_{i,j}-\frac{h_1}{2},\xi_{i,j}+\frac{h_1}{2}]\times[\eta_{i,j}-\frac{h_2}{2},\eta_{i,j}+\frac{h_2}{2}]$ in the computational domain.

Note that the singular integrals in Eqs. (2.14) and (2.15) are integrable in the sense of Cauchy principal value. The summations in Eqs. (3.10) and (3.11) give leading order approximations to these integrals in which the singular integrals over the small cells when $(i_1,j_1)=(i,j)$ are neglected. The errors of such approximations are $\mathcal{O}(h_1\ln h_1+h_2\ln h_2)$.

The approximations of the singular integrals over these small cells are derived in the appendix, and will reduce the errors to $\mathcal{O}(h_1^2\ln h_1+h_2^2\ln h_2)$ if they are included in Eqs. (3.10) and (3.11), respectively, to approximate the corresponding integral expressions of σ_{13} and σ_{23} in Eqs. (2.14) and (2.15). However, the full expressions of these higher order correction terms are quite lengthy, see the appendix. Instead, we keep only a few second order derivative terms of ϕ and ψ in $(s_1)_{i,j}$ and $(s_2)_{i,j}$ that help to stabilize the numerical scheme. The errors after incorporation of these terms will still be $\mathcal{O}(h_1\ln h_1+h_2\ln h_2)$. When x and y are locally linear functions of ξ and η, respectively, the errors after incorporation of these terms will be reduced to $\mathcal{O}(h_1^2+h_2^2)$.

The adopted expressions for these singular integrals are

$$\begin{aligned}(s_1)_{i,j}\approx&-(\phi_{xx})_{i,j}\frac{\mu}{4\pi(1-\nu)}\int_{D^p_{i,j}}\frac{(x_{i,j}-x_1)^2}{[(x_{i,j}-x_1)^2+(y_{i,j}-y_1)^2]^{3/2}}dx_1dy_1\\&-(\phi_{yy})_{i,j}\frac{\mu}{4\pi}\int_{D^p_{i,j}}\frac{(y_{i,j}-y_1)^2}{[(x_{i,j}-x_1)^2+(y_{i,j}-y_1)^2]^{3/2}}dx_1dy_1\\&-(\psi_{xy})_{i,j}\frac{\mu\nu}{4\pi(1-\nu)}\int_{D^p_{i,j}}\frac{(x_1-x_{i,j})^2}{[(x_{i,j}-x_1)^2+(y_{i,j}-y_1)^2]^{3/2}}dx_1dy_1\end{aligned}\tag{3.14}$$

and

$$\begin{aligned}(s_2)_{i,j}\approx&-(\psi_{xx})_{i,j}\frac{\mu}{4\pi}\int_{D_{i,j}^p}\frac{(x_{i,j}-x_1)^2}{[(x_{i,j}-x_1)^2+(y_{i,j}-y_1)^2]^{3/2}}dx_1dy_1\\&-(\psi_{yy})_{i,j}\frac{\mu}{4\pi(1-\nu)}\int_{D_{i,j}^p}\frac{(y_{i,j}-y_1)^2}{[(x_{i,j}-x_1)^2+(y_{i,j}-y_1)^2]^{3/2}}dx_1dy_1\\&-(\phi_{xy})_{i,j}\frac{\mu\nu}{4\pi(1-\nu)}\int_{D_{i,j}^p}\frac{(y_1-y_{i,j})^2}{[(x_{i,j}-x_1)^2+(y_{i,j}-y_1)^2]^{3/2}}dx_1dy_1,\end{aligned}\tag{3.15}$$

where

$$\begin{aligned}&\int_{D_{i,j}^p}\frac{(x_1-x_{i,j})^2}{[(x_{i,j}-x_1)^2+(y_{i,j}-y_1)^2]^{3/2}}dx_1dy_1\\\approx&h_1\left(\frac{J}{\sqrt{x_\eta^2+y_\eta^2}}\right)_{i,j}\Big[\sin(\theta_2-\theta_3)+\sin(\theta_1+\theta_3)\\&+\frac{\sin^2\theta_3}{2}\ln\frac{(1+\sin(\theta_2+\theta_3))(1+\sin(\theta_1-\theta_3))}{(1-\sin(\theta_2+\theta_3))(1-\sin(\theta_1-\theta_3))}\Big]+h_2\left(\frac{J}{\sqrt{x_\xi^2+y_\xi^2}}\right)_{i,j}\Big[\sin(\theta_2-\theta_4)\\&-\sin(\theta_1+\theta_4)+\frac{\sin^2\theta_4}{2}\ln\frac{(1-\sin(\theta_1-\theta_4))(1+\sin(\theta_2+\theta_4))}{(1+\sin(\theta_1-\theta_4))(1-\sin(\theta_2+\theta_4))}\Big],\end{aligned}\tag{3.16}$$

$$\begin{aligned}&\int_{D_{i,j}^p}\frac{(y_1-y_{i,j})^2}{[(x_{i,j}-x_1)^2+(y_{i,j}-y_1)^2]^{3/2}}dx_1dy_1\\\approx&h_1\left(\frac{J}{\sqrt{x_\eta^2+y_\eta^2}}\right)_{i,j}\Big[-\sin(\theta_2-\theta_3)-\sin(\theta_1+\theta_3)\\&+\frac{\cos^2\theta_3}{2}\ln\frac{(1+\sin(\theta_2+\theta_3))(1+\sin(\theta_1-\theta_3))}{(1-\sin(\theta_2+\theta_3))(1-\sin(\theta_1-\theta_3))}\Big]+h_2\left(\frac{J}{\sqrt{x_\xi^2+y_\xi^2}}\right)_{i,j}\Big[\sin(\theta_1+\theta_4)\\&-\sin(\theta_2-\theta_4)+\frac{\cos^2\theta_4}{2}\ln\frac{(1-\sin(\theta_1-\theta_4))(1+\sin(\theta_2+\theta_4))}{(1+\sin(\theta_1-\theta_4))(1-\sin(\theta_2+\theta_4))}\Big],\end{aligned}\tag{3.17}$$

and

$$\begin{aligned}&\theta_1=\left(\tan^{-1}\frac{-y_\xi h_1+y_\eta h_2}{x_\xi h_1-x_\eta h_2}\right)_{i,j},\quad\theta_2=\left(\tan^{-1}\frac{y_\xi h_1+y_\eta h_2}{x_\xi h_1+x_\eta h_2}\right)_{i,j},\\&\theta_3=\left(\tan^{-1}\frac{x_\eta}{y_\eta}\right)_{i,j},\quad\theta_4=\left(\tan^{-1}\frac{x_\xi}{y_\xi}\right)_{i,j}.\end{aligned}\tag{3.18}$$

4 Numerical examples

In this section, we present test examples using our numerical method for a generalized Peierls-Nabarro model based on the fast multipole method and the iterative grid redistribution. We focus on the core structures of straight dislocations and dislocation loops on the (111) planes of fcc Al and Cu. The values of related physical parameters of Al and Cu are given in the last paragraph of Section 2. We also present numerical examples of a straight dislocation on the interface of epitaxial thin film and substrate.

4.1 A straight dislocation

We first apply our adaptive numerical method to a straight dislocation, and compare the result with that of the available analytic formula and those obtained on uniform meshes.

We consider a straight edge dislocation. The dislocation is lying along the y-axis. The Burgers vector is in the x direction. Following the setting of the available analytic formula, we only consider the disregistry component ϕ which is the component in the direction of the Burgers vector, and use the Frenkel sinusoidal potential $\gamma(\phi)=\frac{\mu b^2}{4\pi^2 d}(1-\cos\frac{2\pi\phi}{b})$, where $d=\sqrt{2/3}b$ is the interplanar distance in the $[111]$ direction. We choose $\nu=0.347$ which is the value of Al. The analytic solution for this edge dislocation is [1]: $\phi(x)=\frac{b}{\pi}\tan^{-1}\frac{x}{\zeta}$, where $\zeta=\frac{d}{2(1-\nu)}$ is the core width of the dislocation.

The physical domain and computational domain in our simulation are $[-\pi,\pi]^2$, for which we choose the length unit such that the length of the Burgers vector is $b=0.3$. Thus the domain size is $L=21b$ in each direction. Periodic boundary condition is used at the domain boundaries in the y direction for the infinite extension of the dislocation in the $+y$ and $-y$ directions. To compute the solution of this one-dimensional problem, the mesh in the y direction is a fine uniform mesh with $N=64$ grid points. Neumann boundary condition is used at the domain boundaries in the x direction to mimic a dislocation in an infinite domain for which analytic formula is available. The computational domain in x direction is discretized into a uniform $M=16$ mesh. We choose the weight function in grid redistribution to be $w=1+|\phi_x|+0.8333b|\phi_{xx}|$, and only redistribute the mesh points in the x direction. The criterion to invoke the grid redistribution process is $\max|\frac{d\phi}{d\tilde{\xi}}|>TOL=2.5b/L$.

We start the evolution from a linear function $\phi(x)$ with increment of b over the x direction of the domain, and the initial mesh on the physical domain is equal to the uniform mesh on the computational domain in the grid redistribution. The disregistry function ϕ converges to an equilibrium state that represents the core structure of the dislocation.

Fig. 2(a) shows the equilibrium dislocation disregistry function $\phi(x)$ obtained using our numerical method and comparison with the available analytic formula. Excellent agreement can be seen from this figure. The center of this dislocation is located at the origin in the figure, and the disregistry function ϕ varies significantly within a small region near the dislocation center, which is the core region of the dislocation. Note that partial

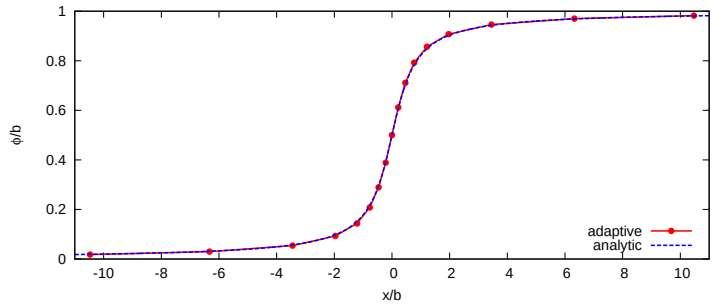

(a)

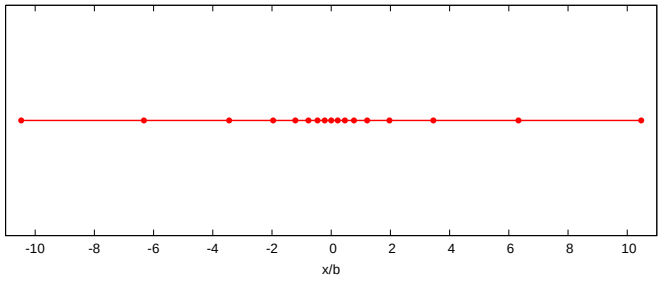

(b)

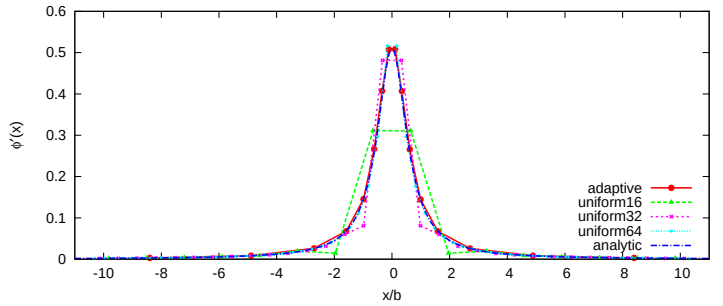

(c)

Figure 2: (a) Equilibrium dislocation disregistry function $\phi(x)$ obtained using our adaptive method with $M=16$ and comparison with the available analytic formula $\phi(x)=\frac{b}{\pi}\tan^{-1}\frac{x}{\zeta}$, where $\zeta=\frac{d}{2(1-\nu)}$, for a straight edge dislocation. Dots: results of our numerical method. Dash line: results of the analytical formula. (b) The redistributed mesh generated for the equilibrium profile of $\phi(x)$ in our calculation shown in (a). (c) The Burgers vector density $\rho(x)=\phi'(x)=\frac{b}{\pi}\frac{\zeta}{x^2+\zeta^2}$ obtained using our adaptive method with $M=16$, and comparisons with the result of analytic formula and those obtained on uniform meshes.

dissociation of dislocations is not included under the setting of this analytic formula.

The final redistributed mesh generated for the equilibrium profile of $\phi(x)$ in our numerical calculation is shown in Fig. 2(b) (see also (a)). As expected, the grid points in the redistributed mesh are concentrated within the core region of the dislocation where $|\phi'(x)|$ is large.

An important application of the Peierls-Nabarro model is that it gives a nonsingular Burgers vector density of the dislocation, which is $\rho(x)=\phi'(x)$ and equals $\frac{b}{\pi}\frac{\zeta}{x^2+\zeta^2}$ in this case. The Burgers vector density does not only describe the core profile of the dislocation, but also leads to accurate nonsingular stress field near the dislocation and nonsingular line energy of the dislocation. The obtained Burgers vector density using our adaptive method and comparison with the analytic formula are shown in Fig. 2(c). The derivative of $\phi(x)$ is calculated by central difference scheme: $\rho(x_{i+\frac{1}{2}})=\phi'(x_{i+\frac{1}{2}})=\frac{\phi(x_{i+1})-\phi(x_i)}{x_{i+1}-x_i}$. It can be seen that our numerical result on the adaptive mesh accurately resolves the regularized-delta-function-shape Burgers vector density $\rho(x)$ even within the dislocation core region.

We have also performed convergence tests on uniform meshes for $\rho(x)$, and the results are also shown in Fig. 2(c). We do see convergence of the numerical results to the analytic formula as the uniform mesh is refined from $M=16$ to 32 and finally to 64. However, the convergence is slow, and the result of the adaptive mesh with $M=16$ grid points is notably more accurate than the result of $M=64$ uniform mesh near the peak of the profile of $\rho(x)$.

4.2 Dislocations near a free surface

Thin film materials play important roles in microelectronic and photonic applications. A thin film is stressed due to the lattice mismatch between the film and the substrate, and can be relaxed by formation of misfit dislocations beyond a critical film thickness. The misfit dislocations stay at the film-substrate interface under the Peach-Koehler force due to misfit stress and the image force due to the free film surface. The core profile of a misfit dislocation is essential to many important properties of the thin film materials such as the critical thickness for the formation of misfit dislocations based on energy calculation [6,7].

We consider a straight edge dislocation parallel to the free film-surface and lying in a slip plane with angle $\alpha_f=\cos^{-1}\frac{1}{\sqrt{3}}$ to the film surface, see Fig. 3(a). The height of the thin film is h_f, and is on an infinite substrate. The x direction is along the slip plane, and the portion in the film is $[-h_f\csc\alpha_f,0]$. Assume that the elastic constants are the same in the film and the substrate, and the Poisson ratio is $\nu=0.25$.

In this case, the disregistry function ϕ is defined for $x\in[-h_f\csc\alpha_f,\infty]$, and the evolution equation is

$$\frac{\partial\phi}{\partial t}=-\left(\sigma_{13}+\frac{\partial\gamma}{\partial\phi}\right), \tag{4.1}$$

where the stress component is given by

$$\sigma_{13}(x)=\frac{\mu}{2\pi(1-\nu)}\int_{x_s}^{\infty}\left\{\frac{1}{x-x_1}\right.$$
$$\left.-\sum_{n=0}^{5}\frac{c_n(x_1-x_s)^n(x-x_s)^{5-n}}{[(x_1-x_s)^2-2(x-x_s)(x_1-x_s)\cos2\alpha_f+(x-x_s)^2]^3}\right\}\phi_x(x_1)dx_1+\sigma_{13}^0\chi_f(x), \tag{4.2}$$

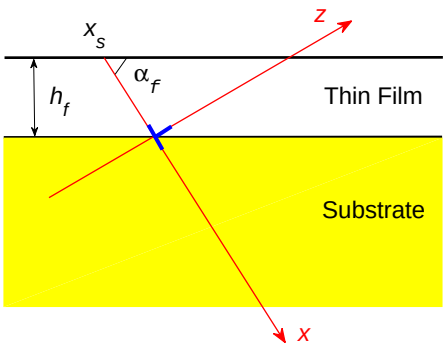

(a)

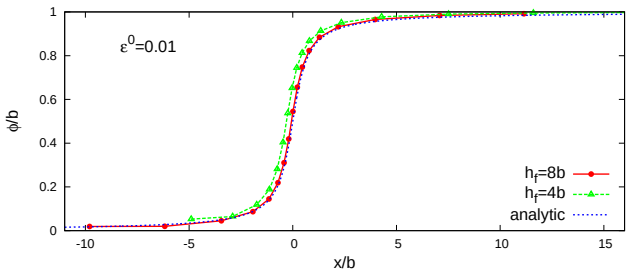

(b)

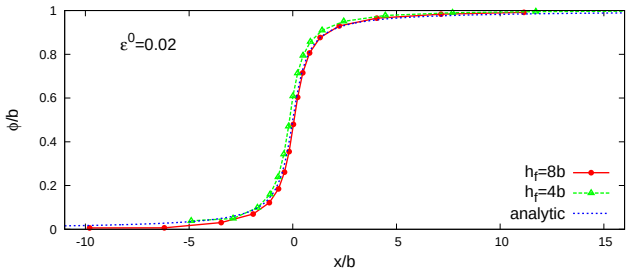

(c)

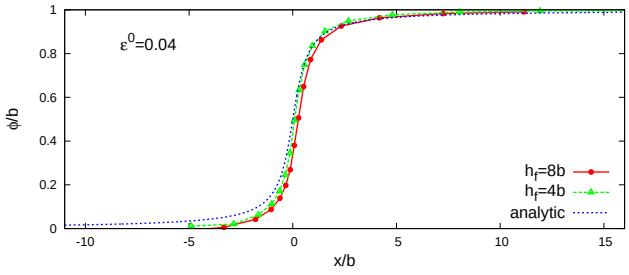

(d)

Figure 3: An edge dislocation located in the film-substrate interface (a), and profiles of the disregistry function ϕ when the misfit $\epsilon^0 = 0.01$ (b), 0.02 (c), and 0.04 (d). The results are compared with the analytic result for a dislocation in an infinite medium.

where $x_s=-h_f\csc\alpha_f$ is the x-coordinate of the intersection point of the slip plane with the film surface, and the Frenkel sinusoidal potential is $\gamma(\phi)=\frac{\mu b^2}{4\pi^2 d}(1-\cos\frac{2\pi\phi}{b})$.

The expression of σ_{13} in Eq. (4.2) consists of the stress in an infinite medium (the $1/(x-x_1)$ term) and the image stress due to the free surface [6, 7, 40] (the rest terms), where the coefficients are

$$c_0=1,\quad c_1=-1-6\cos2\alpha_f+2\cos^2 2\alpha_f,\quad c_2=6-2\cos2\alpha_f+6\cos^2 2\alpha_f,$$
$$c_3=-6\cos2\alpha_f-4\cos^3 2\alpha_f,\quad c_4=-3+2\cos2\alpha_f+6\cos^2 2\alpha_f,\quad c_5=1-2\cos^2 2\alpha_f. \tag{4.3}$$

The term $\sigma^0_{13}\chi_f(x)$ in Eq. (4.2) comes from the constant misfit stress in the film, where

$$\chi_f(x)=\begin{cases} 1, & -h_f\csc\alpha_f\le x\le 0,\\ 0, & \text{otherwise,}\end{cases} \tag{4.4}$$

and

$$\sigma^0_{13}=\sigma^0\sin\alpha_f\cos\alpha_f,\quad \sigma^0=2\mu\frac{1+\nu}{1-\nu}\epsilon^0. \tag{4.5}$$

Here ϵ^0 is the misfit due to the lattice mismatch between the film and the substrate.

We choose the simulation domain to be $[-h_f\csc\alpha_f,-h_f\csc\alpha_f+L]$, where the size of the domain is $L=21b$. (Numerically, the computational domain is $[-h_f\csc\alpha_f,-h_f\csc\alpha_f+2\pi]$, where $b=0.3$.) Neumann boundary condition is used on the domain boundaries. We focus on the grid redistribution in this example, and use direct summation for the calculation of the integral in the total stress field in Eq. (4.2). The adaptive mesh has $M=16$ grid points and the same numerical treatments as in the previous example. The FMM implementation and grid redistribution can be readily applied to more general dislocations near free surfaces, in which proper boundary conditions and more numerical treatments for the image force are needed when the dislocations intersect the free surfaces [38, 39, 41, 42]. Such generalization will be explored in the future work.

Fig. 3(b) and (c) show the obtained disregistry function ϕ for different thin film height $h_f=4b,8b$ and different misfit $\epsilon^0=0.01,0.02,0.04$, as well as comparisons with the analytical formula in an infinite medium. In each case, we can see that the grid points in the redistributed mesh are concentrated within the core region of the dislocation where $|\phi'(x)|$ is large. The misfit dislocation stays near the film-substrate interface ($x=0$) under the image force due to the free film surface, which attracts the dislocation towards the free surface, and the Peach-Koehler force due to the misfit stress, which pushes the dislocation away from the free surface when it is in the thin film. Fig. 3(b) shows the results when the misfit $\epsilon^0=0.01$. The image force is stronger than the force due to misfit stress in the case $h_f=4b$, and the dislocation is attracted to the free surface (compared with the analytical formula in an infinite medium). Whereas the two forces are almost balanced in the case of $h_f=8b$, and deviation of ϕ from the analytic formula in an infinite medium without these two forces is small. When the misfit ϵ^0 increases to 0.02 (Fig. 3(c)) and further to 0.04 (Fig. 3(d)), the Peach-Koehler force due to misfit stress becomes stronger,

the disregistry function ϕ in the film is reduced further towards the value 0, leading to smaller dislocation core width on the side of the film ($x<0$). Note that there is no misfit stress in the substrate ($x>0$). When the misfit $\epsilon^0=0.04$, the Peach-Koehler force due to misfit stress is even stronger, instead of further reducing the dislocation core width, the dislocation center in the case of $h_f=8b$ is pushed slightly into the substrate from the film-substrate interface.

4.3 Dislocation loops

In this subsection, we report the simulation results of the core structure of dislocation loops in Al and Cu. The dislocation loops are in the xy plane which represents the (111) crystallography plane. The x-axis is in the $[\bar{1}10]$ direction which is in the direction of the Burgers vector **b**, and the y-axis is in the $[\bar{1}\bar{1}2]$ direction. The center of a loop is located at the origin. We use the full generalized stacking fault energy in Eq. (2.17) which enables partial dissociation for the dislocation core structure.

The physical domain and the computational domain in our simulation are $[-\pi,\pi]^2$, for which we choose the length unit such that the length of the Burgers vector is $b=0.15$. Thus the domain size is $L=42b$ in each direction. Neumann boundary condition is used at the domain boundaries to mimic a dislocation loop in an infinite medium. The computational domain is discretized into a uniform 64×64 mesh. We choose the weight function in the grid redistribution to be $w=\sqrt{1+0.02(\phi/\phi^{(0)}_{\max})^2+0.02(|\nabla_p\,\phi|/\phi^{(1)}_{\max})^2+0.02(|\Delta_p\phi|/\phi^{(2)}_{\max})^2}$, where $\phi^{(0)}_{\max}$, $\phi^{(1)}_{\max}$ and $\phi^{(2)}_{\max}$ are the maximum values of $|\phi|$, $|\nabla_p\,\phi|$ and $|\Delta_p\phi|$, respectively, over the physical domain. The criterion to invoke the grid redistribution process is $\max|\nabla_c\,\phi|>TOL=5b/(L/2)$.

To obtain the core structure of a dislocation loop, a constant shear stress is needed to prevent the loop from shrinking as in Ref. [21]. The resulting unstable equilibrium configuration gives local maximum of the total energy. In order to obtain this unstable configuration of the dislocation loop, a Lagrange multiplier is used to keep the area enclosed by a dislocation loop constant during the energy minimization. The control area is proportional to the integral of the disregistry component ϕ which is in the direction of the Burgers vector. That is, we minimize the total energy in Eq. (2.8) subject to the constraint $\int_{R^2}\phi(x,y,t)dxdy=A_0$, where $A_0=\int_{R^2}\phi(x,y,0)dxdy$. Using the method of Lagrange multiplier, we look for the stationary solution of the functional

$$E^\lambda=E_{\text{elastic}}+E_{\text{misfit}}+\lambda\left(\int_{R^2}\phi dxdy-A_0\right), \tag{4.6}$$

which is found by solving the following evolution equations to equilibrium:

$$\frac{\partial\phi}{\partial t}=-M\left(\sigma_{13}+\frac{\partial\gamma}{\partial\phi}+\lambda\right),$$

$$\frac{\partial \psi}{\partial t} = -M\left(\sigma_{23} + \frac{\partial \gamma}{\partial \psi}\right),$$
$$\frac{\partial \lambda}{\partial t} = M_\lambda\left(\int_{R^2} \phi dxdy - A_0\right), \tag{4.7}$$

where M and M_λ are some positive constants. Comparing with the equilibrium conditions in Eq. (2.12), it can be seen that the resulting Lagrange multiplier λ is equal to the constant applied stress σ_{13}^{app}.

In the two examples of dislocation loops in Al and Cu, the initial conditions in the evolution are $\phi = b$ inside a circle and 0 outside with smooth transition in between, and $\psi = 0$ over the domain. This configuration represents a circular dislocation loop. The radius of the initial circular loop is $R = 11b$.

The initial mesh on the physical domain is equal to the uniform mesh on the computational domain in the grid redistribution. The disregistry functions ϕ and ψ together with the constant applied stress converge to an equilibrium state that represents the core structure of a dislocation loop that encloses the same area as the initial circular loop. The dislocation core region is identified by the region between the contour lines of $\phi = \frac{1}{4}b$ and $\phi = \frac{3}{4}b$ [21].

The core profile of a dislocation loop in Al is shown in Fig. 4. This loop is in (unstable) equilibrium with the applied stress $\sigma_{13}^{\text{app}} = 0.040\mu$. Fig. 4(a) and (b) show the disregistry component ϕ along the x direction and y direction, respectively. This disregistry component is in the direction of the Burgers vector and determines the dislocation loops. Fig. 4(c) and (d) show the disregistry component ψ along the x direction and y direction, respectively. This disregistry component is in the direction perpendicular to the Burgers vector, and enables dislocation partial dissociation in the Peierls-Nabarro model. It can be seen that the values of ψ are very small compared with the values of ϕ for this dislocation loop in Al.

The dislocation core region is shown in Fig. 4(e). These two contour lines are also the locations of the partial dislocations (Shockley partials) of the dislocation loop [1]. We can see that in this dislocation loop in Al, the two Shockley partials are not clearly separated, only some tendency of splitting is shown, which agrees with the theoretical prediction [1]. This dislocation loop is elongated in the direction of the Burgers vector (the x direction), which agrees with the classical dislocation theory that the edge dislocations have larger line energy than the screw dislocations [1]. These simulation results also agree with previous results obtained using periodic boundary conditions [21].

The final redistributed mesh in the physical domain generated for the equilibrium state of this dislocation loop in Al is shown in Fig. 4(f). It can be seen that the grid points in the redistributed mesh are indeed concentrated within the core region of this dislocation loop.

Now we examine the obtained applied stress $\sigma_{13}^{\text{app}} = 0.040\mu$ that maintains this dislocation loop. This unstable equilibrium state is the result of balance between the line tension force which tends to shrink the loop, and the Peach-Koehler force due to the applied

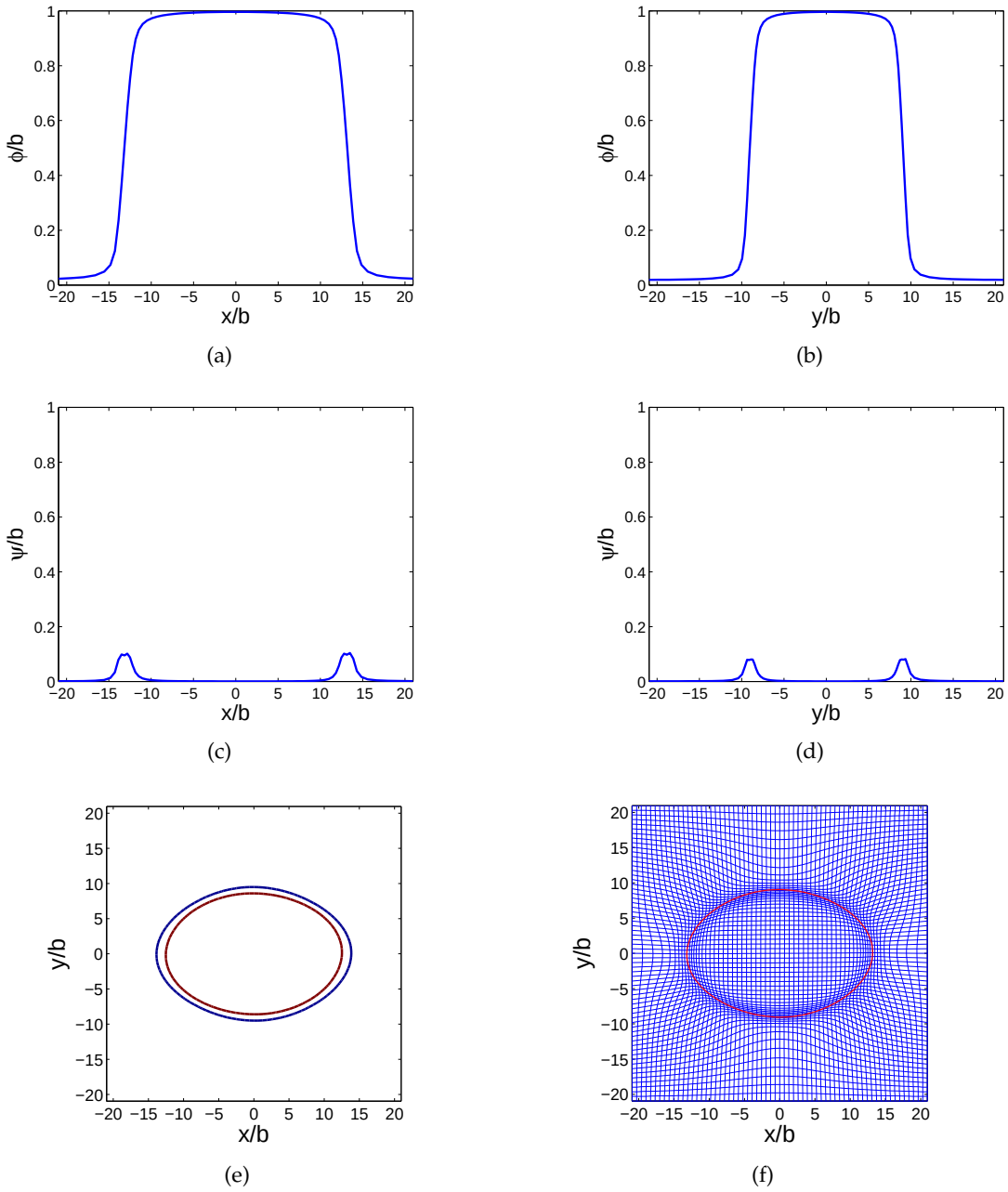

Figure 4: Core structure of a dislocation loop in Al. (a) Disregistry ϕ along the x-axis. (b) Disregistry ϕ along the y-axis. (c) Disregistry ψ along the x-axis. (d) Disregistry ψ along the y-axis. (e) Core region and locations of the two Shockley partials of this dislocation loop. (f) Grid distribution in the physical domain. Since the two Shockley partials are very close to each other, we only plot the center of the core region of the dislocation loop which is identified by the contour line of $\phi = b/2$ in (f). The Burgers vector $\mathbf{b}$ is in the x direction.

stress which tends to expand it. The line tension force at the point where the dislocation is screw is approximately [1, 43]

$$T = \frac{\mu b^2(1+\nu)}{4\pi(1-\nu)} \frac{1}{R_s} \ln \frac{4R_s}{b}, \tag{4.8}$$

where R_s is the curvature radius at the screw point and the dislocation core radius is b. To estimate the value of this line tension force, we approximate the dislocation loop by an ellipse, see Fig. 4(e), and the major and minor axes of the ellipse are $a_1 = 13b$ and $a_2 = 9b$, respectively. At a screw point, the curvature radius is approximately $R_s = a_1^2/a_2 = 19b$. This gives an estimate of the line tension force of $T = 0.037\mu b$, which agrees excellently with the Peach-Koehlor force $\sigma_{13}^{\text{app}} b = 0.040\mu b$.

The core profile of a dislocation loop in Cu is shown in Fig. 5. This loop is in (unstable) equilibrium with the applied stress $\sigma_{13}^{\text{app}} = 0.052\mu$. Fig. 5(a)-(d) show the disregistry components ϕ and ψ along the x- and y-axes. Unlike the dislocation loop in Al in Fig. 4, the two Shockley partials of a dislocation loop in Cu, identified by the contour lines of $\phi = \frac{1}{4}b$ and $\phi = \frac{3}{4}b$, respectively, are clearly separated. Between the two partial loops is the stacking fault region, which is an energy local minimum state of the generalized stacking fault energy in Eq. (2.17) with $(\phi, \psi) = (\frac{1}{2}b, \frac{\sqrt{3}}{6}b)$. The locations of the two Shockley partial loops of this dislocation loop in Cu are plotted in Fig. 5(e). The wide separation of the two Shockley partials agrees with the theoretical prediction [1]. It is also interesting to see from Fig. 5(e) that the two partial loops of the perfect loop in Cu are elongated approximately in the directions of their own Burgers vectors, respectively. This behavior is quite different from that of the undissociated or slightly dissociated perfect loops in Al in Fig. 4(e), in which the two partial loops together with the perfect loops are all elongated in the direction of the Burgers vector of the perfect loops. These simulation results also agree with previous results obtained using periodic boundary conditions [21].

Fig. 5(e) also shows the final redistributed mesh in the physical domain generated for the equilibrium state of this dislocation loop in Cu. In this case, the grid points in the redistributed mesh are concentrated near the locations of the two Shockley partial loops where the disregistry component ϕ changes rapidly. From Fig. 4(f) and Fig. 5(e), one can see that our numerical method successfully generates the desired adaptive meshes for the two different behaviors of the disregistry function ϕ for dislocation loops in Al and Cu.

5 Summary

We have presented a numerical method for a generalized Peierls-Nabarro model for curved dislocations [21], based on the fast multipole method [33, 34] and the iterative grid redistribution [35]. The fast multipole method enables the calculation of the long-range elastic interaction within operations that scale linearly with the total number of grid points. The iterative grid redistribution places more mesh nodes in the regions

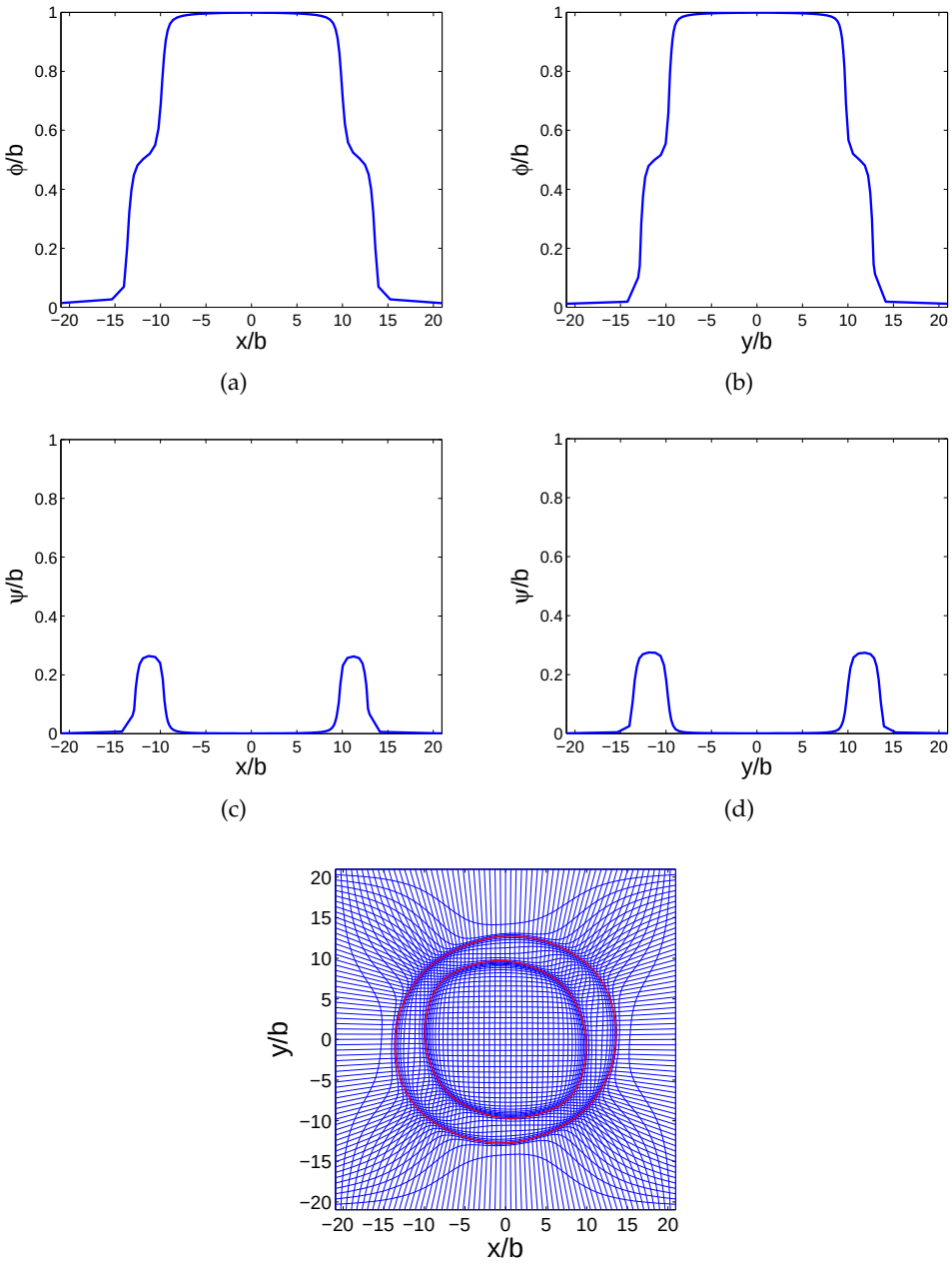

Figure 5: Core structure of a dislocation loop in Cu. (a) Disregistry ϕ along the x-axis. (b) Disregistry ϕ along the y-axis. (c) Disregistry ψ along the x-axis. (d) Disregistry ψ along the y-axis. (e) Core region and locations of the two Shockley partials of this dislocation loop, and grid distribution in the physical domain. The Burgers vector $\mathbf{b}$ is in the x direction.

around the dislocations than in the rest of the domain, thus increases the accuracy and efficiency. This numerical method has an overall computational cost of $\mathcal{O}(N)$, where N is the total number of numerical grid points, thus it significantly improves the available methods in which the long-range stress fields are calculated by direct summations with $\mathcal{O}(N^2)$ operations [7,10,13,15–18]. Compared with the previous FFT based method [21], this new method is more flexible to handle problems with general boundary conditions.

We have presented numerical examples using this method on the core structure of dislocations in Al and Cu, whose core regions are very narrow and wide, respectively. In both cases, our numerical method is able to generate the desired adaptive meshes with grid points concentrated mainly within the regions where the disregistry function changes rapidly. We have also presented numerical examples of the core profile of a straight dislocation on the interface of epitaxial thin film and substrate, where the image stress due to the free surface is not negligible.

This numerical method can be generalized to dislocations in anisotropic medium [21]. It can also be applied to more general dislocations near free surfaces, in which proper boundary conditions and more numerical treatments for the image force are needed when the dislocations intersect the free surfaces [38,39,41,42]. These generalizations and applications of the developed numerical methods will be explored in the future work.

Acknowledgments

This work is partially supported by Hong Kong University of Science and Technology RPC07/08.SC15 and Hong Kong Research Grants Council General Research Fund 603807. The author CJ is supported by the Zhejiang Provincial Natural Science Foundation of China (No. LY13A010014). The authors thank Prof. Xiao-Ping Wang of Hong Kong University of Science and Technology for helpful discussion on the iterative grid redistribution method.

Appendix: Approximations of local singular integrals

In this appendix, we calculate the approximations of the integrals in $(\sigma_{13})_{i,j}$ and $(\sigma_{23})_{i,j}$ in Eqs. (2.14) and (2.15) over the small region $D^p_{i,j}$ containing the point $(x_{i,j},y_{i,j})$ and mapped from the small region $(\xi_1,\eta_1)\in D^c_{i,j}=[\xi_{i,j}-\frac{h_1}{2},\xi_{i,j}+\frac{h_1}{2}]\times[\eta_{i,j}-\frac{h_2}{2},\eta_{i,j}+\frac{h_2}{2}]$ in the computational domain, denoted by $(s_1)_{i,j}$ and $(s_2)_{i,j}$, respectively. These integrals contain singular integrands which require special treatment in numerical approximation. If $(s_1)_{i,j}$ and $(s_2)_{i,j}$ are added, respectively, in Eqs. (3.10) and (3.11), the numerical errors of $(\sigma_{13})_{i,j}$ and $(\sigma_{23})_{i,j}$ will be reduced from $\mathcal{O}(h_1\ln h_1+h_2\ln h_2)$ to $\mathcal{O}(h_1^2\ln h_1+h_2^2\ln h_2)$.

We first approximate these singular integrals using Taylor expansions of the partial derivatives of ϕ and ψ at the point $(x_{i,j},y_{i,j})$. For example, for the first term in Eq. (2.14),

we have

$$\begin{aligned}
&\frac{\mu}{4\pi}\int_{D_{i,j}^p}\frac{y_{i,j}-y_1}{[(x_{i,j}-x_1)^2+(y_{i,j}-y_1)^2]^{3/2}}\phi_y(x_1,y_1)dx_1dy_1\\
=&\frac{\mu}{4\pi}\int_{D_{i,j}^p}\frac{y_{i,j}-y_1}{[(x_{i,j}-x_1)^2+(y_{i,j}-y_1)^2]^{3/2}}\Big[(\phi_y)_{i,j}+(\phi_{xy})_{i,j}(x_1-x_{i,j})+(\phi_{yy})_{i,j}(y_1-y_{i,j})\\
&\quad+\mathcal{O}\big(|x_1-x_{i,j}|^2+|y_1-y_{i,j}|^2\big)\Big]dx_1dy_1\\
=&-(\phi_y)_{i,j}\frac{\mu}{4\pi}\int_{D_{i,j}^p}\frac{y_1-y_{i,j}}{[(x_{i,j}-x_1)^2+(y_{i,j}-y_1)^2]^{3/2}}dx_1dy_1\\
&-(\phi_{xy})_{i,j}\frac{\mu}{4\pi}\int_{D_{i,j}^p}\frac{(x_1-x_{i,j})(y_1-y_{i,j})}{[(x_{i,j}-x_1)^2+(y_{i,j}-y_1)^2]^{3/2}}dx_1dy_1\\
&-(\phi_{yy})_{i,j}\frac{\mu}{4\pi}\int_{D_{i,j}^p}\frac{(y_1-y_{i,j})^2}{[(x_{i,j}-x_1)^2+(y_{i,j}-y_1)^2]^{3/2}}dx_1dy_1+\mathcal{O}(h_1^2+h_2^2).
\end{aligned}\tag{A.1}$$

Summarizing the approximations of all the terms, we have

$$\begin{aligned}
(s_1)_{i,j}\approx&-\Big[(\phi_x)_{i,j}+\nu(\psi_y)_{i,j}\Big]\frac{\mu}{4\pi(1-\nu)}\int_{D_{i,j}^p}\frac{x_1-x_{i,j}}{[(x_{i,j}-x_1)^2+(y_{i,j}-y_1)^2]^{3/2}}dx_1dy_1\\
&-(\phi_y)_{i,j}\frac{\mu}{4\pi}\int_{D_{i,j}^p}\frac{y_1-y_{i,j}}{[(x_{i,j}-x_1)^2+(y_{i,j}-y_1)^2]^{3/2}}dx_1dy_1\\
&-\Big[(\phi_{xx})_{i,j}+\nu(\psi_{xy})_{i,j}\Big]\frac{\mu}{4\pi(1-\nu)}\int_{D_{i,j}^p}\frac{(x_1-x_{i,j})^2}{[(x_{i,j}-x_1)^2+(y_{i,j}-y_1)^2]^{3/2}}dx_1dy_1\\
&-(\phi_{yy})_{i,j}\frac{\mu}{4\pi}\int_{D_{i,j}^p}\frac{(y_1-y_{i,j})^2}{[(x_{i,j}-x_1)^2+(y_{i,j}-y_1)^2]^{3/2}}dx_1dy_1\\
&-\Big[(2-\nu)(\phi_{xy})_{i,j}+\nu(\psi_{yy})_{i,j}\Big]\frac{\mu}{4\pi(1-\nu)}\int_{D_{i,j}^p}\frac{(x_1-x_{i,j})(y_1-y_{i,j})}{[(x_{i,j}-x_1)^2+(y_{i,j}-y_1)^2]^{3/2}}dx_1dy_1,
\end{aligned}\tag{A.2}$$

and

$$\begin{aligned}
(s_2)_{i,j}\approx&-(\psi_x)_{i,j}\frac{\mu}{4\pi}\int_{D_{i,j}^p}\frac{x_1-x_{i,j}}{[(x_{i,j}-x_1)^2+(y_{i,j}-y_1)^2]^{3/2}}dx_1dy_1\\
&-\Big[\nu(\phi_x)_{i,j}+(\psi_y)_{i,j}\Big]\frac{\mu}{4\pi(1-\nu)}\int_{D_{i,j}^p}\frac{y_1-y_{i,j}}{[(x_{i,j}-x_1)^2+(y_{i,j}-y_1)^2]^{3/2}}dx_1dy_1\\
&-(\psi_{xx})_{i,j}\frac{\mu}{4\pi}\int_{D_{i,j}^p}\frac{(x_1-x_{i,j})^2}{[(x_{i,j}-x_1)^2+(y_{i,j}-y_1)^2]^{3/2}}dx_1dy_1
\end{aligned}$$

$$-\left[\nu(\phi_{xy})_{i,j}+(\psi_{yy})_{i,j}\right]\frac{\mu}{4\pi(1-\nu)}\int_{D_{i,j}^p}\frac{(y_1-y_{i,j})^2}{[(x_{i,j}-x_1)^2+(y_{i,j}-y_1)^2]^{3/2}}dx_1dy_1$$
$$-\left[\nu(\phi_{xx})_{i,j}+(2-\nu)(\psi_{xy})_{i,j}\right]\frac{\mu}{4\pi(1-\nu)}\int_{D_{i,j}^p}\frac{(x_1-x_{i,j})(y_1-y_{i,j})}{[(x_{i,j}-x_1)^2+(y_{i,j}-y_1)^2]^{3/2}}dx_1dy_1. \quad (A.3)$$

The second partial derivatives in these expressions can be calculated by repeating the first partial derivative formulas in Eq. (3.12), in which the partial derivatives with respect to ξ and η are calculated using the central difference scheme. The errors of these approximations are of $\mathcal{O}(h_1^2+h_2^2)$.

It can be seen from Eqs. (A.2) and (A.3) that we only need to calculate the following five integrals over $D_{i,j}^p$:

$$\int_{D_{i,j}^p}\frac{x_1-x_{i,j}}{[(x_{i,j}-x_1)^2+(y_{i,j}-y_1)^2]^{3/2}}dx_1dy_1,$$
$$\int_{D_{i,j}^p}\frac{y_1-y_{i,j}}{[(x_{i,j}-x_1)^2+(y_{i,j}-y_1)^2]^{3/2}}dx_1dy_1,$$
$$\int_{D_{i,j}^p}\frac{(x_1-x_{i,j})^2}{[(x_{i,j}-x_1)^2+(y_{i,j}-y_1)^2]^{3/2}}dx_1dy_1,$$
$$\int_{D_{i,j}^p}\frac{(y_1-y_{i,j})^2}{[(x_{i,j}-x_1)^2+(y_{i,j}-y_1)^2]^{3/2}}dx_1dy_1,$$
$$\int_{D_{i,j}^p}\frac{(x_1-x_{i,j})(y_1-y_{i,j})^2}{[(x_{i,j}-x_1)^2+(y_{i,j}-y_1)^2]^{3/2}}dx_1dy_1.$$

We denote $\bar{D}_{i,j}^p$ to be the parallelogram that approximates the small cell $D_{i,j}^p$ with boundaries

$$x_1=x_{i,j}+(x_\xi)_{i,j}(\xi_1-\xi_{i,j})+(x_\eta)_{i,j}(\eta_1-\eta_{i,j}),$$
$$y_1=y_{i,j}+(y_\xi)_{i,j}(\xi_1-\xi_{i,j})+(y_\eta)_{i,j}(\eta_1-\eta_{i,j}), \quad (A.4)$$

where $\xi_1-\xi_{i,j}=\pm\frac{h_1}{2}$ or $\eta_1-\eta_{i,j}=\pm\frac{h_2}{2}$, see Fig. 6. Using polar coordinates of the xy plane, it can be calculated that

$$\int_{D_{i,j}^p}\frac{(x_1-x_{i,j})^2}{[(x_{i,j}-x_1)^2+(y_{i,j}-y_1)^2]^{3/2}}dx_1dy_1$$
$$\approx\int_{\bar{D}_{i,j}^p}\frac{(x_{i,j}-x_1)^2}{[(x_{i,j}-x_1)^2+(y_{i,j}-y_1)^2]^{3/2}}dx_1dy_1$$

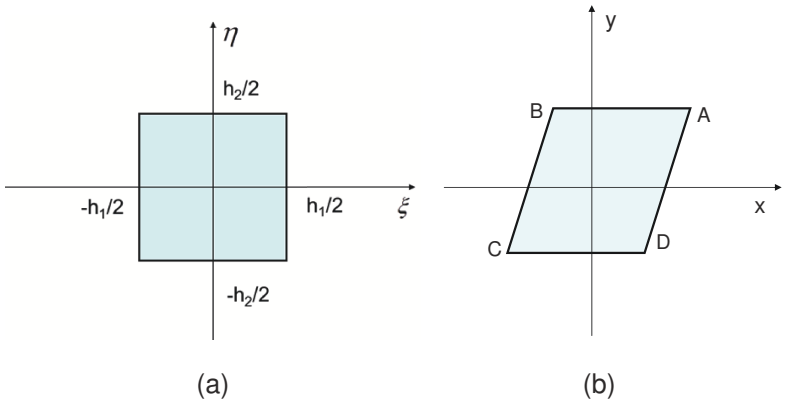

Figure 6: Domains over which the local singular integrals in Eqs. (A.5)-(A.7) are evaluated. (a) The small region $D^c_{i,j}=[\xi_{i,j}-\frac{h_1}{2},\xi_{i,j}+\frac{h_1}{2}]\times[\eta_{i,j}-\frac{h_2}{2},\eta_{i,j}+\frac{h_2}{2}]$ in the computational domain. The center of the region is $(\xi_{i,j},\eta_{i,j})$. (b) In the physical domain, the parallelogram $\bar{D}^p_{i,j}$ is used to approximate the exact domain $D^p_{i,j}$ mapped from the small region $D^c_{i,j}$ in (a). The center of the parallelogram is $(x_{i,j}(\xi_{i,j},\eta_{i,j}),y_{i,j}(\xi_{i,j},\eta_{i,j}))$.

$$
\begin{aligned}
&=h_1\left(\frac{J}{\sqrt{x_\eta^2+y_\eta^2}}\right)_{i,j}\Big[\sin(\theta_2-\theta_3)+\sin(\theta_1+\theta_3)\\
&\quad+\frac{\sin^2\theta_3}{2}\ln\frac{(1+\sin(\theta_2+\theta_3))(1+\sin(\theta_1-\theta_3))}{(1-\sin(\theta_2+\theta_3))(1-\sin(\theta_1-\theta_3))}\Big]+h_2\left(\frac{J}{\sqrt{x_\xi^2+y_\xi^2}}\right)_{i,j}\Big[\sin(\theta_2-\theta_4)\\
&\quad-\sin(\theta_1+\theta_4)+\frac{\sin^2\theta_4}{2}\ln\frac{(1-\sin(\theta_1-\theta_4))(1+\sin(\theta_2+\theta_4))}{(1+\sin(\theta_1-\theta_4))(1-\sin(\theta_2+\theta_4))}\Big],
\end{aligned}
\tag{A.5}
$$

$$
\begin{aligned}
&\int_{D^p_{i,j}}\frac{(y_1-y_{i,j})^2}{[(x_{i,j}-x_1)^2+(y_{i,j}-y_1)^2]^{3/2}}dx_1dy_1\\
&\approx\int_{\bar{D}^p_{i,j}}\frac{(y_{i,j}-y_1)^2}{[(x_{i,j}-x_1)^2+(y_{i,j}-y_1)^2]^{3/2}}dx_1dy_1\\
&=h_1\left(\frac{J}{\sqrt{x_\eta^2+y_\eta^2}}\right)_{i,j}\Big[-\sin(\theta_2-\theta_3)-\sin(\theta_1+\theta_3)\\
&\quad+\frac{\cos^2\theta_3}{2}\ln\frac{(1+\sin(\theta_2+\theta_3))(1+\sin(\theta_1-\theta_3))}{(1-\sin(\theta_2+\theta_3))(1-\sin(\theta_1-\theta_3))}\Big]+h_2\left(\frac{J}{\sqrt{x_\xi^2+y_\xi^2}}\right)_{i,j}\Big[\sin(\theta_1+\theta_4)\\
&\quad-\sin(\theta_2-\theta_4)+\frac{\cos^2\theta_4}{2}\ln\frac{(1-\sin(\theta_1-\theta_4))(1+\sin(\theta_2+\theta_4))}{(1+\sin(\theta_1-\theta_4))(1-\sin(\theta_2+\theta_4))}\Big],
\end{aligned}
\tag{A.6}
$$

$$
\begin{aligned}
&\int_{D_{i,j}^p} \frac{(x_1-x_{i,j})(y_1-y_{i,j})}{[(x_{i,j}-x_1)^2+(y_{i,j}-y_1)^2]^{3/2}}dx_1dy_1\\
\approx&\int_{\bar{D}_{i,j}^p} \frac{(x_1-x_{i,j})(y_1-y_{i,j})}{[(x_{i,j}-x_1)^2+(y_{i,j}-y_1)^2]^{3/2}}dx_1dy_1\\
=&h_1\left(\frac{J}{\sqrt{x_\eta^2+y_\eta^2}}\right)_{i,j}\Bigg[\cos(\theta_1+\theta_3)-\cos(\theta_2-\theta_3)\\
&-\frac{\sin2\theta_3}{4}\ln\frac{(1+\sin(\theta_2+\theta_3))(1+\sin(\theta_1-\theta_3))}{(1-\sin(\theta_2+\theta_3))(1-\sin(\theta_1-\theta_3))}\Bigg]+h_2\left(\frac{J}{\sqrt{x_\xi^2+y_\xi^2}}\right)_{i,j}\Bigg[-\cos(\theta_2-\theta_4)\\
&-\cos(\theta_1+\theta_4)-\frac{\sin2\theta_4}{4}\ln\frac{(1-\sin(\theta_1-\theta_4))(1+\sin(\theta_2+\theta_4))}{(1+\sin(\theta_1-\theta_4))(1-\sin(\theta_2+\theta_4))}\Bigg],
\end{aligned}
\tag{A.7}
$$

where the expressions of θ_1, θ_2, θ_3, and θ_4 are given by Eq. (3.18).

In order to evaluate the rest two singular integrals, we denote $\hat{D}_{i,j}^p$ to be the higher order approximation of the small cell $D_{i,j}^p$ with curved boundaries

$$
\begin{aligned}
x_1=&x_{i,j}+(x_\xi)_{i,j}(\xi_1-\xi_{i,j})+(x_\eta)_{i,j}(\eta_1-\eta_{i,j})\\
&+\frac{1}{2}(x_{\xi\xi})_{i,j}(\xi_1-\xi_{i,j})^2+\frac{1}{2}(x_{\eta\eta})_{i,j}(\eta_1-\eta_{i,j})^2+(x_{\xi\eta})_{i,j}(\xi_1-\xi_{i,j})(\eta_1-\eta_{i,j}),\\
y_1=&y_{i,j}+(y_\xi)_{i,j}(\xi_1-\xi_{i,j})+(y_\eta)_{i,j}(\eta_1-\eta_{i,j})\\
&+\frac{1}{2}(y_{\xi\xi})_{i,j}(\xi_1-\xi_{i,j})^2+\frac{1}{2}(y_{\eta\eta})_{i,j}(\eta_1-\eta_{i,j})^2+(y_{\xi\eta})_{i,j}(\xi_1-\xi_{i,j})(\eta_1-\eta_{i,j}),
\end{aligned}
\tag{A.8}
$$

where $\xi_1-\xi_{i,j}=\pm\frac{h_1}{2}$ or $\eta_1-\eta_{i,j}=\pm\frac{h_2}{2}$. It can be evaluated using polar coordinates of the xy plane that

$$
\begin{aligned}
&\int_{D_{i,j}^p} \frac{x_1-x_{i,j}}{[(x_{i,j}-x_1)^2+(y_{i,j}-y_1)^2]^{3/2}}dx_1dy_1\\
\approx&\int_{\hat{D}_{i,j}^p} \frac{x_1-x_{i,j}}{[(x_{i,j}-x_1)^2+(y_{i,j}-y_1)^2]^{3/2}}dx_1dy_1\\
\approx&-\frac{\cos\theta_1}{2}\ln\frac{h_1(x_\xi\sin\theta_1-y_\xi\cos\theta_1)}{h_2(y_\eta\cos\theta_1-x_\eta\sin\theta_1)}\\
&\cdot\frac{(\frac{1}{2}x_{\xi\xi}h_1^2+\frac{1}{2}x_{\eta\eta}h_2^2-x_{\xi\eta}h_1h_2)(y_\xi h_1-y_\eta h_2)-(\frac{1}{2}y_{\xi\xi}h_1^2+\frac{1}{2}y_{\eta\eta}h_2^2-y_{\xi\eta}h_1h_2)(x_\xi h_1-x_\eta h_2)}{(x_\xi h_1-x_\eta h_2)^2+(y_\xi h_1-y_\eta h_2)^2}
\end{aligned}
$$

$$
\begin{aligned}
&-\frac{\cos\theta_2}{2}\ln\frac{h_1(x_\xi\sin\theta_2-y_\xi\cos\theta_2)}{h_2(y_\eta\cos\theta_2-x_\eta\sin\theta_2)}\\
&\cdot\frac{-(\frac{1}{2}x_{\xi\xi}h_1^2+\frac{1}{2}x_{\eta\eta}h_2^2+x_{\xi\eta}h_1h_2)(y_\xi h_1+y_\eta h_2)+(\frac{1}{2}y_{\xi\xi}h_1^2+\frac{1}{2}y_{\eta\eta}h_2^2+y_{\xi\eta}h_1h_2)(x_\xi h_1+x_\eta h_2)}{(x_\xi h_1+x_\eta h_2)^2+(y_\xi h_1+y_\eta h_2)^2},
\end{aligned}
\tag{A.9}
$$

$$
\begin{aligned}
&\int_{D_{i,j}^p}\frac{y_1-y_{i,j}}{[(x_{i,j}-x_1)^2+(y_{i,j}-y_1)^2]^{3/2}}dx_1dy_1\\
\approx&\int_{\hat{D}_{i,j}^p}\frac{y_1-y_{i,j}}{[(x_{i,j}-x_1)^2+(y_{i,j}-y_1)^2]^{3/2}}dx_1dy_1\\
\approx&-\frac{\sin\theta_1}{2}\ln\frac{h_1(x_\xi\sin\theta_1-y_\xi\cos\theta_1)}{h_2(y_\eta\cos\theta_1-x_\eta\sin\theta_1)}\\
&\cdot\frac{(\frac{1}{2}x_{\xi\xi}h_1^2+\frac{1}{2}x_{\eta\eta}h_2^2-x_{\xi\eta}h_1h_2)(y_\xi h_1-y_\eta h_2)-(\frac{1}{2}y_{\xi\xi}h_1^2+\frac{1}{2}y_{\eta\eta}h_2^2-y_{\xi\eta}h_1h_2)(x_\xi h_1-x_\eta h_2)}{(x_\xi h_1-x_\eta h_2)^2+(y_\xi h_1-y_\eta h_2)^2}\\
&-\frac{\sin\theta_2}{2}\ln\frac{h_1(x_\xi\sin\theta_2-y_\xi\cos\theta_2)}{h_2(y_\eta\cos\theta_2-x_\eta\sin\theta_2)}\\
&\cdot\frac{-(\frac{1}{2}x_{\xi\xi}h_1^2+\frac{1}{2}x_{\eta\eta}h_2^2+x_{\xi\eta}h_1h_2)(y_\xi h_1+y_\eta h_2)+(\frac{1}{2}y_{\xi\xi}h_1^2+\frac{1}{2}y_{\eta\eta}h_2^2+y_{\xi\eta}h_1h_2)(x_\xi h_1+x_\eta h_2)}{(x_\xi h_1+x_\eta h_2)^2+(y_\xi h_1+y_\eta h_2)^2}.
\end{aligned}
\tag{A.10}
$$

In summary, the approximations of the local singular terms $(s_1)_{i,j}$ and $(s_2)_{i,j}$ are given by Eqs. (A.2), (A.3) and (A.5), (A.6), (A.7), (A.9), (A.10). The errors are $\mathcal{O}(h_1^2\ln h_1+h_2^2\ln h_2)$.

References

[1] J.P. Hirth, J. Lothe, Theory of Dislocations, 2nd ed., John Wiley, New York, 1982.
[2] R.E. Peierls, The size of a dislocation, Proc. Phys. Soc. 52 (1940) 34-37.
[3] F.R.N. Nabarro, Dislocations in a simple cubic lattice, Proc. Phys. Soc. 59 (1947) 256-272.
[4] V. Vitek, Intrinsic stacking faults in body-centered cubic crystals, Phil. Mag. 18 (1968) 773-786.
[5] E. Kaxiras and M.S. Duesbery, Free energies of generalized stacking faults in Si and implications for the brittle-ductile transition, Phys. Rev. Lett. 70 (1993) 3752-3755.
[6] A.P. Payne, W.D. Nix, B.M. Lairson, and B.M. Clemens, Strain relaxation in ultrathin films: A modified theory of misfit-dislocation energetics, Phys. Rev. B 47 (1993), 13730-13736.
[7] G.E. Beltz and L.B. Freund, Analysis of the strained-layer critical thickness concept based on a Peierls-Nabarro model of a threading dislocation, Phil. Mag. A 69 (1994) 183-202.
[8] G. Schoeck, The generaliezd Peierls-Nabarro model, Phil. Mag. A 69 (1994) 1085-1095.
[9] B. Joos and M.S. Duesbery, The Peierls stress of dislocations: An analytic formula, Phys. Rev. Lett. 78 (1997) 266-269.
[10] V.V. Bulatov and E. Kaxiras, Semi-discrete variational Peierls framework for dislocation core properties, Phys. Rev. Lett. 78 (1997) 4221-4223.

[11] J. Hartford, B. von Sydow, G. Wahnstrom and B.I. Lundqvist, Peierls barriers and stresses for edge dislocations in Pd and Al calculated from first principles, Phys. Rev. B 58 (1998) 2487-2496.
[12] O.N. Mryasov, Y.N. Gornostyrev and A.J. Freeman, Generalized stacking-fault energetics and dislocation properties: Compact versus spread unit-dislocation structures in TiAl and CuAu, Phys. Rev. B 58 (1998) 11927-11932.
[13] A.B. Movchan, R. Bullough and J.R. Willis, Stability of a dislocation: Discrete model, Eur. J. Appl. Math. 9 (1998) 373-396.
[14] G. Schoeck, The Peierls energy revisited, Phil. Mag. A 79 (1999) 2629-2636.
[15] G. Lu, N. Kioussis, V.V. Bulatov and E. Kaxiras, Generalized-stacking-fault energy surface and dislocation properties of aluminum, Phys. Rev. B 62 (2000) 3099-3108.
[16] G. Xu and A.S. Argon, Homogeneous nucleation of dislocation loops under stress in perfect crystals, Phil. Mag. Lett. 80 (2000) 605-611.
[17] G. Lu, V.V. Bulatov and N. Kioussis, Dislocation constriction and cross-slip: an ab initio study, Phys. Rev. B 66, (2002) 144103.
[18] A.B. Movchan, R. Bullough and J.R. Willis, Two-dimensional lattice models of the Peierls type, Phil. Mag. 83 (2003) 569-587.
[19] G. Schoeck and M. Krystian, The peierls energy and kink energy in fcc metals, Phil. Mag. 85 (2005) 949-966.
[20] Y. Xiang, Modeling dislocations at different scales, Commun. Comput. Phys. 1(2006) 383-424.
[21] Y. Xiang, H. Wei, P.B. Ming and W. E, A generalized Peierls-Nabarro model for curved dislocations and core structures of dislocation loops in Al and Cu, Acta Mater. 56 (2008) 1447-1460.
[22] H. Wei, Y. Xiang and P.B. Ming, A generalized Peierls-Nabarro model for curved dislocations using discrete Fourier transform, Commun. Comput. Phys. 4 (2008) 275-293.
[23] H. Wei and Y. Xiang, A generalized Peierls-Nabarro model for kinked dislocations Phil. Mag. 89 (2009) 2333-2354.
[24] S.Y. Dai, Y. Xiang, and T.Y. Zhang, A continuum model for core relaxation of incoherent twin boundaries based on the Peierls-Nabarro framework, Scripta Mater. 64 (2011), 438-441.
[25] G. Schoeck, The core structure and Peierls potential of dislocations in Al, Mater. Sci. Eng. A 558 (2012), 162-169.
[26] Y. Kamimura, K. Edagawa, and S. Takeuchi, Experimental evaluation of the Peierls stresses in a variety of crystals and their relation to the crystal structure, Acta Mater. 61 (2013), 294-309.
[27] S.Y. Dai, Y. Xiang, and D. J. Srolovitz, Structure and energy of (111) low angle twist boundaries in Al, Cu and Ni, Acta Mater. 61 (2013), 1327-1337.
[28] S.Y. Dai, Y. Xiang, and D. J. Srolovitz, Atomistic, generalized Peierls-Nabarro, and analytical models for (111) twist boundaries in Al, Cu and Ni for all twist angles, Acta Mater., 69 (2014), 162-174.
[29] C. Shen, J. Li, and Y. Wang, Microscopic phase field model for dislocation core and grain boundary, preprint, 2013.
[30] G. Xu and M. Ortiz, A variational boundary integral method for the analysis of 3D cracks of arbitrary geometry modeled as continuous distributions of dislocation loops, Int. J. Numer. Meth. Engng. 36 (1993) 3675-3701.
[31] J.F. Nye, Some geometrical relations in dislocated crystals, Acta Metall. 1 (1953), 153-162.
[32] J.A. Zimmerman, H. Gao, and F.F. Abraham, Generalized stacking fault energies for embed-

ded atom FCC metals, Modell. Simul. Mater. Sci. Eng. 8 (2000), 103-115.
[33] L. Greengard and V. Rokhlin, A new version of the Fast Multipole Method for the Laplace equation in three dimensions, Acta Numerica 6 (1997), 229-269.
[34] D.G. Zhao, J.F. Huang, and Y. Xiang, A new version fast multipole method for evaluating the stress field of dislocation ensembles, Modelling Simul. Mater. Sci. Eng. 18 (2010), 045006.
[35] W. Ren and X.P. Wang, An iterative grid redistribution method for singular problems in multiple dimensions, J. Comput. Phys. 159 (2000) 246-273.
[36] A. Winslow, Numerical solution of the quasi-linear Poisson equation, J. Comput. Phys. 1 (1966), 149-172.
[37] E. Van der Giessen and A. Needleman, Discrete dislocation plasticity: a simple planar model, Model. Simul. Mater. Sci. Eng. 3 (1995), 689-735.
[38] S.S. Quek, Y. Xiang, Y.W. Zhang, D.J. Srolovitz, and C. Lu, Level set simulation of dislocation dynamics in thin films, Acta Mater. 54 (2006), 2371-2381.
[39] D.G. Zhao, J.F. Huang, and Y. Xiang, Fast multipole accelerated boundary integral equation method for evaluating the stress field associated with dislocations in a finite medium, Commun. Comput. Phys. 12 (2012), 226-246.
[40] L.B. Freund and D.M. Barnett, A two-dimensional analysis of surface deformation due to dip-slip faulting, Bull. Seism. Soc. Am. 66 (1976), 667-675.
[41] R.W. Balluffi, Introduction to Elasticity Theory for Crystal Defects, Cambridge University Press, Cambridge, 2012.
[42] J. Lothe, The image force on dislocations at free surfaces – Comments on the concept of line tension. In: Fundamental aspects of dislocation theory, vol. 1. National Bureau of Standards (US) Special Publication 317, 1970. pp. 11-22.
[43] R.W. Lardner, Mathematical Theory of Dislocations and Fracture, University of Toronto Press, Toronto, 1974.